The Near-Infrared Broad Emission Line Region of Active Galactic Nuclei – I. The Observations

Hermine Landt[1]

Harvard-Smithsonian Center for Astrophysics, 60 Garden Street, Cambridge, MA 02138.

Misty C. Bentz[1]

Department of Astronomy, The Ohio State University, 140 West 18th Avenue, Columbus, OH 43210.

Martin J. Ward[1]

Department of Physics, University of Durham, South Road, Durham, DH1 3LE, UK.

Martin Elvis[1]

Harvard-Smithsonian Center for Astrophysics, 60 Garden Street, Cambridge, MA 02138.

Bradley M. Peterson

Department of Astronomy, The Ohio State University, 140 West 18th Avenue, Columbus, OH 43210.

Kirk T. Korista

Department of Physics, Western Michigan University, 1903 W. Michigan Avenue, Kalamazoo, MI 49008.

Margarita Karovska

Harvard-Smithsonian Center for Astrophysics, 60 Garden Street, Cambridge, MA 02138.

ABSTRACT

We present high quality (high signal-to-noise ratio and moderate spectral resolution) near-infrared (near-IR) spectroscopic observations of 23 well-known broad-emission line active galactic nuclei (AGN). Additionally, we obtained simultaneous (within two months) optical spectroscopy of similar quality. The near-IR broad emission line spectrum of AGN is dominated by permitted transitions of hydrogen, helium, oxygen, and calcium, and by the rich spectrum of singly-ionized iron. In this paper we present the spectra, line identifications and measurements, and address briefly some of the important issues regarding the physics of AGN broad emission line regions. In particular, we investigate the excitation mechanism of neutral oxygen and confront for the first time theoretical predictions of the near-IR iron emission spectrum with observations.

Subject headings: galaxies: active - galaxies: Seyfert - infrared: galaxies - quasars: emission lines

1. Introduction

Strangely, the near-infrared (near-IR) spectra of broad-emission line active galactic nuclei (type 1 AGN) have been mostly ignored in this new era of infrared spectroscopy. The broad ($\sim 1\% - 5\%$ the speed of light) emission lines observed in the optical and ultraviolet (UV) spectra of these type 1 AGN are the most direct tracers of the activity and immediate environment of supermassive black holes. However, despite 30 years of intensive spectrophotometric studies the geometry and kinematics of the broad emission line region (BELR) remains ill-defined. It is not clear whether the BELR gas has a spherical or disk-like distribution, and whether it consists of a large number of discrete clouds or is part of an outflowing, continuous gas distribution such as an accretion disk wind (see, e.g., review by Sulentic et al. 2000). The knowledge of the BELR geometry and kinematics is essential not only to our understanding of the relation between different types of AGN but also to studies that use the broad emission line widths to estimate black holes masses. These estimates would not be meaningful if the BELR was in outflow, and, if the gas was gravitationally bound but distributed in a disk, the resulting values would be underestimated for sources viewed face-on.

Our current, limited knowledge of the BELR physical conditions and scales was gained primarily through the application of sophisticated photoionization models to the observed emission line intensities and ratios (see, e.g., review by Ferland 2003) and through reverberation mapping studies of the (correlated) continuum and line variability (see, e.g., review by Peterson 1993). Both of these methods have relied so far on spectroscopic observations at optical and UV frequencies. Our goal is to extend these studies to the near-IR wavelengths.

Infrared broad emission lines offer several advantages: (i) since each emission line is formed most efficiently at a particular density and distance from the ionizing source (Baldwin et al. 1995), it is important to incorporate in photoionization and reverberation mapping studies multiple emission lines to map the entire BELR. In this respect, the near-IR broad emission lines are a vital addition to the lines observed at optical and UV frequencies; (ii) the near-IR broad emission lines trace mainly the low-ionization line (LIL) region, a region believed to have extreme properties such as very high densities ($n > 10^{11}$ cm^{-3}) and a disk-like structure (Collin-Souffrin & Lasota 1988; Marziani et al. 1996). However, these properties were derived mainly based on observations of the two strongest Balmer lines, Hα and Hβ, and need additional verification; (iii) the near-IR broad emission lines are little affected by reddening and, therefore, can yield information on the amount of dust present in the BELR when compared to the optical Balmer lines; and (iv) coordinated spectroscopic observations at different wavelengths, which are necessary to cover simultaneously a large number of emission lines in the variable AGN, are easiest to realize at optical and near-IR frequencies.

An additional strong motivation for our observing program was to identify nearby AGN with near-IR broad emission lines sufficiently luminous to allow imaging with the newly commissioned and future near-IR interferometers, such as, e.g., *VLTI* and *Ohana*. The combination of an interferometric map and a reverberation-based velocity-delay map can be expected to yield the BELR structure and kinematics with almost no ambiguity (e.g., Gallimore et al. 2001). In the longer term we will also use these studies to measure the metric of the Universe by purely geometrical means, following Elvis & Karovska (2002). As these authors pointed out, by using reverberation mapping to measure the linear size and the three-dimensional structure of the BELR and an interferometer to measure its angular size it is possible to solve the triangle (as in stellar parallax), giving the angular diameter distance to the quasar. Mapping out angular diameter distance versus redshift gives the metric, and quasars are common and bright up to high redshifts ($z \sim 3$), where the difference between $\Lambda = 0.7$ and $\Lambda = 0.0$ reaches 40%.

This paper presents near-IR spectra of a relatively large sample (23 sources) of type 1 AGN and is the first to include complementary contemporaneous optical spectra to allow the evaluation of commonly measured broad emission line ratios. We concentrate here on the detailed description of our near-IR and optical spectroscopic observations (Section 2), line identifications (Section 3), and flux and velocity width measurements of the most important near-IR and optical broad emis-

sion lines (Section 4). In Section 5 we briefly discuss our results in the context of the general BELR physics. The detailed theoretical analysis of these data will be presented in a series of forthcoming papers.

2. The Observations

We selected for observations well-known AGN with broad emission lines at redshifts such that most of the strong Paschen hydrogen lines fall in the near-IR atmospheric windows. In addition we required that our sources are bright enough in the near-IR (magnitudes $J \lesssim 14$ mag) to allow us to obtain high signal-to-noise ratio (S/N ~ 100) spectra in a reasonable amount of exposure time. As of June 2006 our observed sample comprises 23 sources. In Table 1 we summarize their general properties.

We observed with the NASA Infrared Telescope Facility (IRTF), a 3 m telescope on Mauna Kea, Hawai'i. We used the SpeX spectrograph (Rayner et al. 2003) set in the short cross-dispersed mode (SXD, $0.8 - 2.4$ μm) and equipped with the $0.8 \times 15''$ slit. This set-up gives an average spectral resolution of full width at half maximum (FWHM) ~ 400 km s^{-1}. Before and/or after each source, we observed a nearby (in position and airmass) A0V star with well-known B and V magnitudes. These stars were used to correct the source spectra for telluric absorption (Vacca et al. 2003) and for flux calibration. Flats and arcs were taken with each source/telluric standard star pair. The data were collected during three observing runs in the period of 2004 May - 2006 June. We had clear skies and seeing in the range of $\sim 0.7 - 1''$ for all nights with the exception of 2006 January 9 and 10 which were affected by clouds and had poor seeing of $\sim 1.5''$. In Table 2 we give the journal of observations.

The SpeX data were reduced using Spextool, an Interactive Data Language (IDL)-based software package developed for SpeX users (Cushing et al. 2004). Spextool carries out all the procedures necessary to produce fully reduced spectra. This includes preparation of calibration frames, processing and extraction of spectra from science frames, wavelength calibration of spectra, telluric correction and flux-calibration of spectra, and merging of the different orders into a single, continuous spectrum. The extraction width was adjusted interactively for each source to include all the flux in the spectral trace. The final spectra were corrected for Galactic extinction using the IRAF task *onedspec.deredden* with input A_V values derived from Galactic hydrogen column densities published by Dickey & Lockman (1990). The results are shown in Fig. 1, where we plot for each source the spectrum with the highest S/N. The spectral fits-files are available for download from the journal as a tar-file.

For all our sources we also obtained contemporaneous (within two months) optical spectroscopy with the FAST spectrograph (Fabricant et al. 1998) at the Tillinghast 1.5 m telescope on Mt. Hopkins, Arizona, in queue-observing mode. We used the 300 l/mm grating and a $3''$ slit. This set-up gives a spectral coverage of $\sim 3720 - 7515$ Å and an average spectral resolution of FWHM ~ 330 km s^{-1}. The slit was rotated to the parallactic angle for all observations. In Table 3 we give the journal of observations.

The FAST data were reduced using standard routines from the IRAF software package. In particular the 2-dimensional spectral files were trimmed, overscan- and bias-subtracted, normalized, rectified and wavelength-calibrated. Subsequently the spectrum was extracted using a width that included all the flux in the trace and the 1-dimensional spectral file flux-calibrated using photometric standard stars observed the same night. The final spectra were corrected for Galactic extinction (see above). The spectral fits-files are available for download from the journal as a tar-file.

3. The Emission Line Identifications

We have identified in our near-IR spectra all observed emission lines, both permitted and forbidden transitions (black and red dotted lines, respectively, in Fig. 1), as well as the rich permitted and forbidden transitions of iron, in particular of Fe II (green and cyan dotted lines, respectively, in Fig. 1). The line identifications were gathered from the literature (e.g., Morris & Ward 1988; Osterbrock et al. 1990; Oliva et al. 1994; Thompson 1995; Osterbrock & Fulbright 1996; Rudy et al. 2000; Vanden Berk et al. 2001; Rodríguez-Ardila et al. 2002a; Sigut & Pradhan 2003; Véron-Cetty et al.

2004; Riffel et al. 2006; Mazzalay & Rodríguez-Ardila 2007) and the vacuum rest-frame wavelengths were taken from the Atomic Line List v2.04[1], with the exception of those of the permitted Fe II multiplets, which were taken from Sigut & Pradhan (2003), and those of molecular hydrogen, which were taken from Riffel et al. (2006).

In Table 4 we summarize the identified emission lines in the near-IR frequency range. For six prominent features we could not find a suitable identification using the Fe II multiplet list of Sigut & Pradhan (2003), but profile comparisons suggest that they are iron emission lines. We discuss these further in Section 5.4.3. We note that an extensive list of optical emission lines can be found in Vanden Berk et al. (2001).

4. The Measurements

We have measured the properties of the most important broad emission lines in the spectra of our sources. In order to obtain accurate measures, we have extracted "pure" broad line profiles which involved the following steps: (i) estimation and subtraction of the continuum; (ii) subtraction of blended emission lines of other elements; (iii) removal of the superposed narrow emission line component; and (iv) modeling and subtraction of the Fe II emission. These steps are discussed in detail in the following subsections.

On the extracted "pure" broad emission line profile we measured the flux, FWHM, and shift. The flux was measured with the IRAF task *onedspec.splot* by integrating the emission in the line, i.e., we did not assume a specific profile. The shift was measured as the velocity difference between the theoretical (vacuum) and observed wavelengths of the emission line center, where the emission line center was measured as the center of the width at half maximum. The instrumental width has not been removed from the FWHM values. All measurements were performed on the redshift-corrected spectrum (i.e., in the object's rest-frame). We note that the redshifts were taken from the NASA/IPAC Extragalactic Database (NED) and, therefore, are likely to be inhomogeneous in their definition of the object's rest-frame.

4.1. The Continuum

We have estimated for each broad emission line a local continuum. This task involved, firstly, defining the limits of the wings of the broad emission line, and, secondly, finding line-free continuum regions to each side of the broad emission line large enough to allow for a reliable fit. Since the emission line widths differ widely in our sources we did not attempt to define global line-free continuum regions but rather adjusted the fitted continuum regions individually for each object (and line) and chose them to be as close as possible to the wings and as large as possible. The local continuum was then fitted with a straight line in f_λ vs. λ space and subsequently subtracted.

4.2. The Blends

We have cleaned the spectrum of narrow emission lines of other elements within ~ 12000 km s^{-1} (approximately the largest half-width at zero intensity observed) of the broad emission line's expected rest-frame wavelength by modeling the features with Gaussians and subtracting them from the spectrum using the IRAF task *onedspec.splot*. When required, narrow emission lines were first deblended using the option 'd' of this task before removal. In the case of the oxygen doublet [O III] $\lambda\lambda 4959, 5007$ we did not assume a Gaussian profile but isolated the emission lines from the spectrum by interpolating the Hβ profile under them.

In the case of the near-IR broad emission line Paϵ, which is heavily blended with the [S III] $\lambda 9531$ narrow emission line, we used either the Paα or Paβ profile (whichever had the higher S/N ratio; mostly this was Paβ) as a template. Both these emission lines are excellent templates since they are observed relatively free of strong blends. We scaled the Paschen template profile to the peak intensity of Paϵ and subtracted it from the blend. From the result we isolated the [S III] profile and in turn subtracted this from the total blend to recover, at least in part, the original broad emission line.

We have also used the Paschen template technique described above for the broad emission line

[1]The Atomic Line List is a compilation by Peter van Hoof and is hosted by the Department of Physics and Astronomy at the University of Kentucky (see http://www.pa.uky.edu/~peter/atomic/)

blends Paγ and He I 1.0830 μm, and Paδ and He II 1.0124 μm. In the case of Paγ and He I, we first subtracted the scaled template profile corresponding to the broad emission line with the highest peak, since the peak of the weaker broad emission line is severely contaminated by flux from the wings of the stronger component.

Similarly, we have used the profile of the (unblended) O I 1.1287 μm broad emission line as a template in order to deblend the O I λ8446 broad emission line from the Ca II triplet. The only exceptions were PDS 456 and H 1821+643, where we used the Paβ profile instead. In PDS 456, the O I 1.1287 μm profile is much narrower than that of O I λ8446, and in H 1821+643, O I 1.1287 μm appears to be blue-shifted relative to O I λ8446 by ~ 1400 km s^{-1}.

4.3.   The Narrow Component

The task *onedspec.splot* was also used to model the narrow component with a Gaussian and remove it from the broad emission line profile. The narrow line profile appears inflected (i.e., it is clearly distinguished from the broad line profile; see, e.g., Mrk 290 in Fig. 2) in 11/23 sources. In these cases the modeling and removal process is straightforward. In another two sources, namely, PG 0844+349 and Ark 120, the broad line profiles (with the exception of those of He I 1.0830 μm) had a broad top, either flat or double-peaked. We interpreted this as indication that the contribution from the narrow line component is negligible and left the observed profiles unchanged.

The broad emission lines of the remaining 10/23 sources were peaked, but the transition between broad and narrow component was not perceptible. In these cases we estimated the contribution of the narrow component to the total profile by fitting to its top part a Gaussian with FWHM equal to that of the narrow emission line [O III] λ5007. This method assumes that the FWHM of [O III] λ5007 is representative of the narrow emission line region (NELR) and subtracts the largest possible flux contribution from this region.

No attempt was made to correct the broad line profiles of IRAS 1750+508 and PDS 456 for the presence of a narrow line component. The [O III] emission lines of IRAS 1750+508 show a very strong blue asymmetry, and those of PDS 456

are very weak and strongly blended with (optical) Fe II.

4.4.   The Fe II Subtraction

Most near-IR broad emission lines suffer from moderate to strong blending with Fe II emission features. The template subtraction process described in Section 4.2 isolates these automatically. However, it is necessary to judge if the isolated profile indeed corresponds to Fe II or rather belongs, in part or entirely, to a different, neighboring emission feature (e.g., to He II 1.0124 μm in the case of Fe II 1.0132 μm) or the wing of the broad emission line in question. To determine this, we compared the isolated profile to the profiles of two near-IR Fe II emission features which are relatively strong and observed unblended, namely, Fe II 1.0502 μm and Fe II 1.1126 μm. The Fe II 1.0502 μm emission feature is in fact a blend of Fe II 1.0491 μm and Fe II 1.0502 μm. However, the former is expected to be weaker than the latter by a factor of ~ 7 (Sigut & Pradhan 2003).

In the optical frequency range the continuum around Hβ, He II λ4686, and Hγ is contaminated by numerous Fe II multiplets which blend together to form a pseudo-continuum. We first subtracted this optical Fe II emission before fitting a local continuum. For this purpose we used the template based on the optical spectrum of I Zw 1 published by Véron-Cetty et al. (2004) and available in electronic format. The method generally used to subtract the Fe II emission from optical spectra was first introduced by Boroson & Green (1992). It consists of creating a spectral sequence by broadening (by convolution with Gaussians) and scaling of the Fe II template, which is subsequently packed together into a three-dimensional cube. This cube is then subtracted from a cube consisting in all three dimensions of the object's spectrum.

In contrast to Boroson & Green (1992), in our cases we found it difficult to decide by eye unambiguously which pair of width and strength of the Fe II template gave the cleanest subtraction. Whereas it was rather clear which was the most appropriate strength, changing the width of the Fe II template (at this strength) by as much as several 1000 km s^{-1} gave only slightly different results. This is due to the fact that the Fe II template "smears out" at larger widths,

which leads to essentially subtracting a straight line over large continuum regions. (However, we note that the resulting differences were more pronounced at smaller widths, and in principle a minimum width could be determined.) This degeneracy was also noted by Vestergaard & Peterson (2005). Therefore, it seems necessary to constrain a priori the width of the Fe II template. We did so by using the widths measured for our unblended near-IR iron emission lines Fe II 1.0502 μm or Fe II 1.1126 μm, whichever had the higher S/N ratio (usually Fe II 1.0502 μm). Three sources have near-IR Fe II emission lines narrower than the width of the Fe II template of 1100 km s^{-1}. In these cases we did not broaden the template. For two sources, namely, H 1821+643 and NGC 5548, we do not observe near-IR Fe II emission (except a weak near-IR Fe II emission 'hump'), but we do observe (weak) optical Fe II emission. In these cases we have not subtracted an Fe II template, but simply fit a local continuum using the spectral ranges $\lambda 4435 - 4445$ Å and $\lambda 5075 - 5085$ Å, where Fe II is expected to be very weak.

In many cases, and especially for strong iron emitters such as, e.g., PDS 456, no satisfactory optical Fe II subtraction using the template of Véron-Cetty et al. (2004) was possible. Strong emission residuals remained in particular in the range $4440 - 4700$ Å and also around Fe II $\lambda 4233$. This is most likely due to the fact that the flux ratios between the individual Fe II emission lines differ from object to object, and thus between our sources and I Zw 1 (see also, e.g., Boroson & Green 1992). Therefore, in order to not leave large amounts of flux unaccounted for, we have re-added the corresponding, subtracted Fe II template to the continuum-subtracted spectrum, and, if present, subtracted the isolated He II $\lambda 4686$ profile, before measuring the Fe II emission in the range $\lambda 4440 - 4700$. The exception was the source NGC 4151 for which we measured the optical Fe II emission directly in the subtracted template, since its Hβ broad emission line has very extended wings stretching out to relatively short wavelengths. We note that measuring instead the flux of Fe II $\lambda 4440 - 4700$ directly in the subtracted template can lead to underestimating it by as much as $\sim 40\%$ and typically by $\sim 15\%$.

4.5. Host Galaxy Absorption

Since our optical spectra were obtained through a rather large aperture in objects with strong host galaxy contribution, the Hγ and He I $\lambda 5876$ emission lines are affected by stellar absorption (see also Crenshaw & Peterson 1985). In these cases we used either the Paα or Paβ profile as a template to interpolate the Hγ profile over the strongest absorption lines (most notably G band at 4300 Å), which, when they add together, can appear rather wide.

The absorption lines contaminating He I $\lambda 5876$ (e.g., Na I $\lambda 5896$) were instead fitted with Gaussians and subtracted. We did not attempt to measure the He I $\lambda 5876$ emission line in PDS 456 and Mrk 590. In both sources this line was strongly absorbed, by telluric bands and by the host galaxy, respectively.

4.6. The Tables

In Table 5 we list our results individually for each measured broad emission line. Sources are omitted from the list if the spectrum did not cover the line. If not the entire broad emission line but more than half of it is covered by the spectrum, we list lower limits on the flux. The fluxes of selected Fe II emission lines are listed in Table 6 and are discussed further in Section 5.4. The fluxes of isolated narrow emission lines of other elements are listed in Table 7.

The main sources of measurement errors on the listed broad emission line parameters are the placement of the continuum and the setting of the extension of an emission line. Both of these depend to a large extent on the S/N of the data but also significantly on the subjective decision of the person conducting the measurements. For these reasons we have not attempted to derive individual errors for our measurements. However, the S/N of our data is relatively high and we estimate the error introduced by this quantity alone to be, e.g., a few per cent for the broad emission line fluxes. Measurement errors for the narrow emission line fluxes are due mainly to the approximation with a Gaussian and the placement of the 'narrow emission line continuum'. The Gaussian fit was adequate in the majority of cases, but in some objects this approximation might not account for all of the flux. In general we estimate that the listed values

are accurate to within $\sim 10\%$.

5. The Near-IR Broad Emission Lines

The electron densities in the BELR are sufficiently high ($n \gtrsim 10^8$ cm^{-3}) that virtually all forbidden lines are collisionally suppressed, therefore, almost only permitted transitions contribute to this emission line region. We find that the near-IR spectra of our sources are dominated by permitted emission lines from few elements, namely, hydrogen, helium, oxygen, calcium, and iron. This is similar to what is observed in the optical frequency range.

5.1. The Hydrogen Emission Lines

The observed near-IR hydrogen emission lines contain transitions from the Paschen and Brackett series. We have measured 5/11 observed Paschen emission lines, namely, Paα to Paϵ (shown in Figs. 2-5), and the strongest observed Brackett emission line, namely, Brγ (shown in Fig. 6). Although seen in the majority of our sources (21/23 objects), we have not measured the second strongest observed Brackett emission line, namely, Brδ, since it is strongly affected by telluric absorption. In the optical spectra of our sources we have measured the three strongest Balmer emission lines, namely, Hα, Hβ, and Hγ.

5.1.1. The Paschen and Balmer Series

The Paα and Paβ emission lines are not only two of the strongest emission lines observed in the near-IR, but they are also relatively free of blending features (only two, mostly weak narrow emission lines contaminate the blue wing of Paβ, see Fig. 2). This makes them valuable tools to probe the physical conditions of the BELR. The optical Balmer emission lines, although stronger, suffer from blending with other features and, at least to some degree, are expected to be affected by dust absorption.

Given this importance of Paα and Paβ, it is worth comparing their widths. We do this in Fig. 7 where we plot separately their broad and narrow components (upper right and lower left filled circles, respectively), the latter plotted only for the cases where it is inflected. Taking the spectral resolution (FWHM ~ 350 km s^{-1}) as an error range (dotted lines), as expected, the widths of these

two emission lines are similar. However, in several sources we observe the Paα emission line close to the atmospheric absorption window and this is reflected in Fig. 7. Whereas the scatter for the narrow component is evenly distributed, the scatter in the broad component measurements is mainly towards smaller values for Paα relative to Paβ. As an example, the two most deviant points at the lower and upper end of the broad component distribution correspond to Ark 564 and NGC 5548, respectively. And, as can be seen from Fig. 2, the Paα broad emission lines in these two sources suffers from extreme atmospheric absorption.

All Paschen emission lines of higher order are strongly blended with emission lines from other elements. In particular, Paγ is strongly blended with He I 1.0830 μm and Fe II 1.0863 μm, and its red wing also with Fe II 1.1126 μm (see Fig. 3). The Paδ emission line is heavily blended with the doublet Fe II $\lambda 9956 + 9998$ on its blue side and with He II 1.0124 μm or, in objects with strong iron emission, Fe II 1.0132 μm and Fe II 1.0174 μm on its red side (see Fig. 4). The strongest narrow emission line in the near-IR, namely, [S III] $\lambda 9531$ contaminates the peak and, therefore, in particular the narrow component of the Paϵ emission line. In addition, in strong iron emitters, Fe II $\lambda 9407$ and Fe II $\lambda 9573$ blend in on the blue side and close to the emission line center, respectively (see Fig. 5).

In Fig. 7 we also compare the widths of the Paschen and Balmer emission lines. We chose to plot Paβ, since this line is observed relatively unaffected by atmospheric absorption, versus the two strongest Balmer emission lines, namely, Hα and Hβ (open triangles and squares, respectively). No significant difference is seen between the emission line widths of Hα and Paβ. However, there is a trend for the widths of the Hβ broad components to be larger than those of the Paβ broad components. This is most likely due to the well-known existence of a "red shelf" in the Hβ broad component (e.g., De Robertis 1985; Marziani et al. 1996), which is believed to be formed, at least in part, by emission from weak Fe II multiplets and He I $\lambda 4922, 5016$ (Véron et al. 2002; Kollatschny et al. 2001). The Hβ "red shelf" is observed in the majority of our sources, and especially the three objects with the largest width differences between the Hβ and Paβ broad com-

ponents, namely, Mrk 876, Mrk 590, and NGC 5548, clearly show this feature.

This study is the first to systematically separate the narrow and broad components for both a large number of emission lines and a relatively large sample of type 1 AGN. Taking the Paβ, Hα, and Hβ emission lines as representative, we find that in the majority of the cases the flux of the narrow component is less than $\sim 10\%$ of the flux of the broad component (Fig. 8, lower panel). Whether the narrow component appears inflected or not is, as expected, independent of the flux ratio between the narrow and broad components and depends only on their relative widths. From Fig. 8, upper panel, we obtain that the narrow component appears inflected when its width is below $\sim 20\%$ of that of the broad component.

5.1.2. Dust Extinction

Although the contribution of the narrow component to the total emission line flux is small compared to that of the broad component (see above), the physical conditions of the NELR are, contrary to those of the BELR, relatively well understood (e.g., Osterbrock & Ferland 2006). Therefore, independent measurements of the narrow component fluxes can yield important constraints on, e.g., the presence of dust within our line of sight which could also affect the BELR.

In Fig. 9 we compare our measured narrow emission line fluxes with the predictions from Case B recombination without dust (lower solid line), and including a dust extinction of $A_{\mathrm{V}} = 1$ and 2 mag (middle and upper solid lines, respectively). The values expected from Case B recombination were calculated using the CLOUDY photoionization simulation code (last described by Ferland et al. 1998) and assuming a temperature of $T = 15000$ K and an electron density of $n_e = 10^4$ cm^{-3}. The A_{V} values were transformed into A_λ values using the analytical expression for the interstellar extinction curve of Cardelli et al. (1989) and assuming a parameter of $R_V = 3.1$. Fig. 9 shows the emission line fluxes normalized such that the flux of the Pa β emission line (the near-IR line measured for all sources) was unity. The Case B curves were normalized such that the $A_{\mathrm{V}} = 1$ mag curve at the wavelength of Pa β was unity. Since the measurement errors for the Pa β data point (roughly the size of the symbol)

correspond roughly to the separation between this curve and those for $A_{\mathrm{V}} = 0$ and 2 mag, this representation simply makes the Pa β data point (and in general the near-IR data points) compatible with Case B recombination, irrespective of the amount of dust.

Fig. 9 shows that the observed narrow emission line ratios can be well reproduced by Case B recombination. The effects of dust, however, are clearly observable only in the Balmer emission line ratios, whereas they cannot be detected at a significant level using the Paschen and Brackett emission lines alone. We then assessed the extinction affecting the NELR in our sources based on which of the plotted curves fitted the Balmer emission lines best. For the large majority of our sources plotted in Fig. 9 (12/18 objects) we obtain that the dust extinction is of the order of $A_{\mathrm{V}} \sim 1$ mag. This average seems to be independent of the type of narrow component (i.e., inflected or estimated). For three sources, namely, Mrk 817, NGC 4151, and NGC 4593, the dust extinction is much below this value, whereas for another three sources, namely, Mrk 876, Ark 564, and HE 1228+013, it appears to be as high as $A_{\mathrm{V}} \sim 2$ mag.

Significant reddening of the narrow emission lines of the order obtained here has been observed before in type 1 AGN. Cohen (1983) measured the reddening in the inflected narrow components of 13 type 1 AGN using two to four Balmer lines. Correcting his values for Galactic extinction we obtain for his sample (which has 5 sources in common with ours) an average of $A_{\mathrm{V}} \sim 1$ mag, similar to our result. Ward et al. (1987) estimated the NELR reddening of four objects, of which two, namely, NGC 3227 and NGC 4151, are included in our sample. These authors obtain on average a higher extinction of $A_{\mathrm{V}} \sim 2$ mag. More recent studies, considering, however, only single objects, obtain values similar to our average (e.g., Crenshaw et al. 2001, 2002).

Given this result, the relevant question for our studies is whether the dust causing the observed extinction of the NELR affects also the broad components. This will depend on the location of the dust, i.e., if it is mixed in with the gas producing the narrow emission lines ("internal dust") or if it is located outside the NELR, e.g., in the host galaxy. Since the covering factor of the narrow emission line clouds is assumed to be very small

(only a few per cent), our line of sight towards the BELR will not necessarily intercept these. However, dust external to the NELR will act like a screen and affect also the smallest scale components such as the BELR and the continuum emitted by the accretion disk. In a future paper we plan to study in detail the continuum spectral energy distributions of our sample, supplementing our simultaneous optical and near-IR observations with UV and X-ray archival observations. This will help determine if the continuum source suffers from similarly strong extinction as the NELR.

5.2. The Helium Emission Lines

The helium transitions observed in the near-IR are by far less numerous than the hydrogen emission lines, with only few lines clearly detectable for both neutral and singly-ionized helium. We have measured the strongest of the near-IR emission lines of neutral helium, namely, He I 1.0830 μm, and also the strongest of the optical emission lines, namely, He I λ5876. The He I 1.0830 μm emission line is blended with Pa γ (and in strong iron emitters also with Fe II 1.0863 μm), but, since it is a strong line, it can be easily separated from this using our template profile technique. The He I λ5876 emission line is affected by host galaxy absorption, and we have corrected for it as described in Section 4.5. Conclusive evidence for the presence of Na I λ5896 in emission is observed only in HE 1228+013. In Fig. 10 we compare the isolated profiles of the two He I emission lines and discuss these further below.

The near-IR (and also optical) He II emission lines, and in particular their broad components, are not only relatively weak, but suffer from strong blending. Therefore, the extraction and measurement of the profiles of these emission lines are best performed on mean and root mean square (rms) spectra. In such spectra the constant or slowly varying components, such as, e.g., the wings of a (blending) broad emission line, do not appear, and the He II emission line can be reliably isolated (e.g., Peterson & Wandel 1999). In a future paper we will present results from our near-IR reverberation mapping campaign and will discuss in detail the profiles of the He II emission lines.

5.2.1. The Kinematics of the BELR

The helium and hydrogen emission lines can be used together to study the velocity structure of the BELR. Since emission lines corresponding to higher ionization potentials are expected to be produced at locations closer to the AGN's central ionizing source than emission lines corresponding to lower ionization potentials (e.g., Peterson 1993; Osterbrock & Mathews 1986, and references therein), helium is expected to emanate from locations closer to the center than those responsible for the hydrogen emission. Thus, comparison of the widths of the helium and hydrogen broad emission lines can give important clues regarding the kinematics of the emitting region.

In Fig. 11 we plot the widths of the two He I emission lines versus those of the hydrogen emission lines Paβ, Hα, and Hβ, separately for their (inflected) narrow and broad components. Fig. 11, left panel, shows that whereas the narrow components of the helium and hydrogen emission lines have similar widths, the broad component of He I λ5876 is significantly wider than that of the hydrogen emission lines. E.g., the average FWHM ratio between the He I λ5876 and Paβ emission lines is $\sim$ 1.5. This result is similar to previous findings (e.g., Osterbrock & Shuder 1982; Shang et al. 2007) and in accordance with the current picture that the BELR is dominated by Keplerian motion in the gravitational field of a central supermassive black hole (e.g., Peterson & Wandel 1999).

On the other hand, the broad component of He I 1.0830 μm has widths rather similar to those of the hydrogen emission lines (Fig. 11, right panel). This is expected since He I 1.0830 μm is one of the most optically thick helium emission lines, and, therefore, its emissivity should drop off significantly with increasing incident photon flux. This then renders the He I 1.0830 μm emission line a less suitable probe of the BELR kinematics than the He I λ5876 emission line.

5.3. The Oxygen Emission Lines

We clearly observe in the near-IR spectra of all our sources two of the strongest emission lines of neutral oxygen, namely, O I λ8446 and O I 1.1287 μm (Fig. 12). Contrary to the hydrogen and helium emission lines discussed in the previous

sections, which result mainly from recombination processes, the observed oxygen transitions are assumed to be the result of Lyβ fluorescence (e.g., Grandi 1980; Rudy et al. 1989). However, it is not clear if other excitation processes can also contribute (Rodríguez-Ardila et al. 2002b). In addition, contrary to hydrogen and helium, neutral oxygen emission is believed to be a pure broad-line phenomenon (Grandi 1980; Morris & Ward 1989).

In the following we report for the first time the detection of narrow components to O I emission lines and address the issue of the O I excitation mechanism. Understanding this mechanism is essential since O I emission lines are believed to be a suitable reddening indicator for the BELR (Netzer & Davidson 1979).

5.3.1. The Presence of Narrow Components

Grandi (1980) was the first to observe the spectral region around O I λ8446 for a relatively large sample of Seyfert 1 galaxies (16 objects) and for three Seyfert 2 galaxies. Based on the lack of a detection of O I λ8446 in the Seyfert 2 galaxies and the lack of a narrow component to O I in intermediate Seyfert galaxies (i.e., in Seyfert galaxies with otherwise inflected narrow components), such as, e.g., NGC 5548 and NGC 4151, he concluded that O I is emitted in the BELR only.

Like Grandi (1980), we do not observe narrow components of the O I emission lines in sources which have hydrogen emission lines with inflected narrow components. However, in all other sources, the O I profiles are similar to those of the *total* hydrogen profiles (Fig. 12). This suggests that O I emission can be produced in the NELR. In support of this interpretation are also the findings of Morris & Ward (1985), who found O I emission in two Seyfert 2 galaxies, namely, NGC 5506 and NGC 7314.

5.3.2. The Excitation Mechanism

There are four excitation mechanisms which can lead to the production of O I λ8446 emission: recombination, collisional excitation, continuum fluorescence, and Lyβ fluorescence (e.g., Grandi 1975, 1980). The O I 1.1287 μm emission line, on the other hand, is believed to be the result of Lyβ fluorescence only.

In order to determine the principal excitation mechanism for O I λ8446 in our sources, we start by comparing the *photon* fluxes of the two oxygen emission lines. If Lyβ fluorescence dominates, every O I λ8446 photon is produced via an O I 1.1287 μm photon, and, therefore, we expect the photon flux ratio between the two oxygen emission lines to be unity. If, however, other processes also contribute, the O I λ8446 emission will be enhanced relative to that of O I 1.1287 μm.

Fig. 13, lower panel, shows the distribution of the photon flux ratios between the broad components of the O I 1.1287 μm and O I λ8446 emission lines. In all sources, with the exception of Mrk 590, this ratio is below unity, indicating that processes other than Lyβ fluorescence contribute to the broad O I λ8446 emission. For Mrk 590 we obtain a photon flux ratio of 1.13. Lyβ fluorescence contributes in our sources between $\sim$20-85% of the broad O I λ8446 emission, with 14/23 sources having a contribution from this process of $\gtrsim$60%. In only three sources does this process not dominate, namely, in PDS 456 ($\sim$20%), Ark 120 ($\sim$40%), and NGC 5548 ($\sim$40%), and in the remaining six sources, namely, Mrk 876, Mrk 110, Mrk 509, Mrk 817, Mrk 290, and NGC 4151, Lyβ fluorescence accounts for only half of the broad O I λ8446 flux.

In Fig. 13, upper panel, we compare for the eight sources with detected narrow O I components the photon flux ratios between the O I 1.1287 μm and O I λ8446 emission lines in the BELR and NELR. Three sources, namely, Mrk 509, H 2106$-$099, and Ark 564, have in both emission line regions similar contributions from Lyβ fluorescence of $\sim$50%, $\sim$65%, and $\sim$75%, respectively. In four other sources, namely, HE 1228+013, Mrk 110, Mrk 335, and H 1934$-$063, the Lyβ fluorescence contribution is higher in the NELR than in the BELR, with the largest differences found for Mrk 110 ($\sim$75% in the NELR vs. $\sim$50% in the BELR) and HE 1228+013 (a larger than unity photon flux ratio of 1.26 in the NELR vs. $\sim$85% in the BELR). For 3C 273 we find a smaller Lyβ fluorescence contribution in the NELR than in the BELR ($\sim$40% vs. $\sim$75%).

Since Lyβ fluorescence cannot account for all of the O I λ8446 emission line flux, neither in the BELR nor in the NELR, which of the other three possible excitation mechanisms could also contribute? This can be best assessed by the pres-

ence or lack of other O I emission lines. Continuum fluorescence implies the presence of lines such as, e.g., O I 1.3165 μm, which is the strongest line produced by this process. Recombination and collisional excitation produce, e.g., O I λ7774 (the quintet counterpart to O I λ8446), with ratios of O I λ7774/λ8446 $\approx$ 1.1 (taking the transition probabilities given in the Atomic Line List v2.04) and $\approx$ 0.3 (Grandi 1980), respectively.

The near-IR spectra of the seven sources in our sample with the highest redshifts cover the spectral region around O I λ7774 and this emission line is clearly detected in all of them (see Fig. 14). O I λ7774 is blended with Fe II λ7712 and an unidentified feature which appears to be itself a blend of emission lines at $\sim$ 7875 Å and $\sim$ 7896 Å (see Section 5.4.3). Therefore, we have measured its flux using the profile of O I 1.1287 μm, similar to the procedure adopted for O I λ8446 (see Section 4.2 for details). The O I 1.3165 μm emission line is convincingly detected in only 5/15 sources with spectral coverage in this region (see Fig. 15). In 3C 273 this line is blended with the red wing of Paβ and we used the O I 1.1287 μm profile to measure it.

In Table 8 we list for a total of nine sources the fluxes for the broad components of O I 1.3165 μm and O I λ7774 (columns (4) and (6), respectively). A narrow component to the O I λ7774 emission line was detected in 3C 273, but not in HE 1228+013. Similarly, O I 1.3165 μm narrow components were detected in 3C 273 and Ark 564, but not in HE 1228+013 and H 1934−063. Of the nine sources listed in Table 8, seven have their broad O I λ8446 emission dominated by Lyβ fluorescence (see column (3)). However, for PDS 456 this process is important only at the $\sim$20% level and for Mrk 876 it accounts for only about half of the broad O I λ8446 flux.

For 3/9 sources, namely, IRAS 1750+508, 3C 273, and HE 1228+013, both O I 1.3165 μm and O I λ7774 were detected, Based on their photon flux ratios relative to O I λ8446, continuum fluorescence seems to contribute only a few per cent and recombination seems to account for the remaining $\sim$ 10 − 20% of the broad O I λ8446 emission line flux. However, for 3C 273 the situation in its NELR is different from that in its BELR. As mentioned above, Lyβ fluorescence accounts for only $\sim$40% of its narrow O I λ8446 emis-

sion, and, whereas continuum fluorescence contributes only a few per cent, collisional excitation seems to be the dominant process. For the narrow components we obtain a photon flux ratio of O I λ7774/λ8446 $\sim$ 0.21, after subtracting the fluorescence contribution off the O I λ8446 flux.

For another 3/9 sources, namely, H 1821+643, Mrk 876, and PDS 456, the spectrum covered the location of both O I 1.3165 μm and O I λ7774, but only O I λ7774 was detected. In H 1821+643 and Mrk 876 recombination seems to account for the remaining $\sim$ 20 − 50% of the broad O I λ8446 emission line flux, but PDS 456 has a photon flux ratio of O I λ7774/λ8446 $\sim$ 0.24 (after subtracting the fluorescence contribution off the O I λ8448 flux), similar to the value expected for collisional excitation.

In PG 0844+349, the spectral region around O I 1.3165 μm was not covered, but the photon flux ratio between O I λ7774 and O I λ8446 indicates that recombination accounts for the remaining broad O I λ8446 flux. On the other hand, in Ark 564 and H 1934−063, the spectral region around O I λ7774 was not covered, but the photon flux ratio between O I 1.3165 μm and O I λ8446 indicates that continuum fluorescence is not as important as recombination or collisional excitation.

In summary, Lyβ fluorescence is the dominant production mechanism of broad O I λ8446 in just over half of our sources (14/23 objects). In roughly a third of our sources (6/23 objects) Lyβ fluorescence accounts for about half of the broad O I λ8446 flux, and in only a few sources it is not the dominant process. In one of these few sources, namely, PDS 456, collisional excitation dominates instead. For six sources we determine that recombination (and not collisional excitation) accounts for the remaining broad O I λ8446 emission line flux. Continuum fluorescence is present, but does not seem to be important.

Rodríguez-Ardila et al. (2002b) were the first to present evidence that Lyβ fluorescence is not the only process contributing to the O I λ8446 emission in AGN. We confirm their result using a sample more than three times as large. Similar to our findings, Rodríguez-Ardila et al. (2002b) concluded that continuum fluorescence does not contribute significantly, but since they had observations of O I λ7774 for only one source they could not determine which of the two, recombination or

collisional excitation, was in general the other important process. Their only source with available O I λ7774 was H 1934−063, which is also part of our sample. This line was covered by their optical spectrum which extended further into the red than ours. For this source they obtain a photon flux ratio of O I λ7774/λ8446 $\sim$ 0.2 (after subtracting the fluorescence contribution off the O I λ8446 flux), suggesting that collisional excitation accounts for the remaining $\sim$30% of the O I λ8446 flux.

Recently, Matsuoka et al. (2007) presented O I λ8446 and O I 1.1287 μm emission line measurements for six quasars. They also concluded that O I λ8446 emission is not produced by Lyβ fluorescence alone and identified collisional excitation as the other important process. However, this result was obtained based on comparisons of their observed O I emission line ratios with predictions from photoionization models, which did not include the contribution from recombination. Thus they could only distinguish between collisional excitation and continuum fluorescence. In addition, we note that for the one source in common with our sample, namely, 3C 273, they measured a similar O I λ8446 flux, but a O I 1.1287 μm flux a factor of $\sim$ 2 lower than our value.

5.4. The Iron Emission Lines

We have detected in our near-IR spectra numerous emission lines from the rich spectrum of singly-ionized iron. Contrary to the Fe II emission lines seen in the UV and optical spectra of AGN, which often blend together and at places form a pseudo-continuum, several near-IR Fe II emission lines can be resolved and studied individually. This is important for at least three reasons: (i) the widths of the resolved near-IR Fe II emission lines can be used to broaden suitable UV and optical templates, which leads to a more reliable iron subtraction and thus measurement of the properties of contaminated features. We have used this method successfully in Section 4.; (ii) the fluxes of the resolved near-IR Fe II emission lines can be used to test theoretical iron emission models. We do this in Section 5.4.1.; and (iii) the profiles of the resolved near-IR Fe II emission lines can be compared to those of emission lines of other elements to help answer the long-standing question of where the iron in AGN is produced and excited (see Section 5.4.2).

5.4.1. Observed vs. Predicted Line Strengths

Theoretical iron flux templates have been developed in recent years in order to alleviate the problems inherent to empirical templates. Such problems are, e.g., the assumption that the source used to construct the template is typical of the AGN population, and the complications introduced by the severe blending of broadened AGN emission lines which makes the isolation of an iron template a difficult task. Furthermore, theoretical iron templates have the advantage that model parameters can be adjusted to fit observations, thus allowing one to constrain the excitation mechanism producing the Fe II spectrum.

The most elaborate theoretical predictions were presented by Sigut & Pradhan (2003). Given the relatively large size of our sample and the quality of our data we can now put these to test. For this purpose we have measured in our spectra the fluxes of six individual near-IR Fe II emission lines and of three blends. In addition, we have measured the flux of the optical Fe II 'hump' in the range 4440-4700 Å as detailed in Section 4 and of the near-IR Fe II 'hump' in the range 8150-8365 Å. Our results are listed in Table 6. Two sources, namely, H 1821+643 and NGC 5548, were omitted from this table since their Fe II emission was weak and only the optical and near-IR emission 'humps' could be convincingly detected. In Table 6 we also give the measured fluxes relative to that of the Fe II 1.0491+1.0502 μm blend. We chose this blend since it is relatively strong and observed unaffected by emission from other elements.

In Table 9 we summarize for the six iron emission lines with the largest statistics, namely, the two Fe II 'humps, Fe II λ9407, Fe II λ9573, Fe II λ9956 + 9998 and Fe II 1.0174 μm, the average flux ratios relative to Fe II 1.0491+1.0502 μm and also relative to Fe II 1.1126 μm. Although not observed in all our sources, we have considered as a consistency check also ratios relative to the Fe II 1.1126 μm emission line, since, contrary to Fe II 1.0491+1.0502 μm, it is not a blend and similarly to this observed relatively free of contaminating emission. We list in Table 9 averages for the whole sample and also considering only those sources with the most reliable Fe II profiles for which all three of the emission lines Fe II λ9956 + 9998, Fe II 1.0491+1.0502 μm,

and Fe II 1.1126 μm were detected (11/21 objects; see also Fig. 16).

The observed means of all considered flux ratios relative to Fe II 1.0491+1.0502 μm are significantly ($\geq 2\sigma$) different from the theoretical value expected by Sigut & Pradhan (2003) for their model A (see their Table 3). The only exception is Fe II λ9407. The most significant deviations are observed for the optical and near-IR Fe II 'humps' and for the Fe II 1.0174 μm emission line. On the other hand, all considered flux ratios relative to Fe II 1.1126 μm are consistent with theoretical predictions. This is also the case for the flux ratio between the optical and near-IR Fe II 'humps'.

The mean ratios of the optical and near-IR Fe II 'humps' relative to Fe II 1.0491+1.0502 μm for the whole sample are larger than the expected value by a factor of ~ 2 (significant at the 6σ and 5σ level, respectively). However, considering only the sources with the most reliable Fe II profiles the significance of the difference between observations and predictions reduces to 2 σ.

The four near-IR Fe II emission lines λ9956 + 9998, 1.0491+1.0502 μm, 1.0174 μm, and 1.1126 μm descend from a common upper multiplet and are collectively termed the "1 μm Fe II lines" (e.g., Rudy et al. 2000). Both the Fe II λ9956 + 9998 and Fe II 1.1126 μm emission line fluxes are observed versus that of Fe II 1.0491+1.0502 μm to be larger than predicted by a factor of ~ 2 (at the 3σ and 4σ level, respectively), irrespective of the sample considered. The most significant discrepancy between theory and observations is found for the Fe II 1.0174 μm emission line. Its flux ratio relative to Fe II 1.0491+1.0502 μm is on average a factor of ~ 5 larger than predicted, significant at the 11σ level. A similar result is obtained if only the sources with the most reliable Fe II profiles are considered. The flux of this line relative to that of Fe II 1.1126 μm is larger than the predicted value by a smaller factor of ~ 2, a result which becomes significant only if the most reliable measurements are considered.

In summary, our observations are consistent with the predictions of Sigut & Pradhan (2003) with two exceptions. The Fe II 1.0491+1.0502 μm emission line flux is either overpredicted by theory or underestimated by our measurements by a factor of ~ 2, and by a similar factor the Fe II 1.0174 μm emission line flux is either underpredicted by

theory or overestimated by our measurements.

Considering in particular the sources with the most reliable Fe II profiles, it is unlikely that we have underestimated the flux of Fe II 1.0491+1.0502 μm by as much as a factor of ~ 2, given that this feature is observed relatively uncontaminated. On the other hand, the measurement of the Fe II 1.0174 μm emission line is complicated by its proximity to the rather strong He II 1.0124 μm emission line. However, in the five sources with the most reliable Fe II profiles considered in Table 9, namely, Mrk 110, H 2106−099, Mrk 335, Ark 564, and H 1934−063, the two profiles are rather well separated (see also Fig. 4). Therefore, it seems more likely that whereas the flux of Fe II 1.0491+1.0502 μm is overpredicted by theory, the flux of Fe II 1.0174 μm is underpredicted, and this by a similar factor of ~ 2. This is possible, if, e.g., the oscillator strengths used by Sigut & Pradhan (2003) for these two lines were in error. The Fe II 1.0491+1.0502 μm blend is dominated by emission from the Fe II 1.0502 μm line, and this line and Fe II 1.0174 μm originate from the same upper level. Therefore, the population of this level seems to have been calculated correctly, but not the depopulation statistics. Alternatively, their computations might have to take into account the importance of collisional transitions among highly excited levels populated by Lyα fluorescence, particularly pseudometastable levels, as suggested by Bautista et al. (2004).

Near-IR Fe II emission line measurements have been published so far for only six AGN. Rudy et al. (2000) and Rudy et al. (2001) find for the sources I Zw 1 and Mrk 478 values of −0.31 and −0.37, respectively, for the logarithmic ratio between the Fe II 1.1126 μm and Fe II 1.0502 μm emission lines, similar to our mean, but they do not measure the Fe II 1.0174 μm emission line flux. However, they call attention to the finding of Rudy et al. (1991) who measured in the emission-line star Lk Hα 101 the Fe II 1.0174 μm flux to be stronger than predicted. The sample of Rodríguez-Ardila et al. (2002a) has 3/4 objects in common with our sample, namely, Mrk 335, Ark 564, and H 1934−063. For these we calculated based on the values given in their Table 2 averages of −0.47±0.04, −0.40±0.06, and −0.06±0.11 for the ratios log Fe II 1.0174 μm/1.0502 μm, log Fe II 1.1126 μm/1.0502 μm, and log Fe II 1.0174

μm/1.1126 μm, respectively, which are similar to our results.

5.4.2. The Iron Emitting Region

Understanding where and how Fe II emission is produced in AGN is important for at least two reasons. Firstly, since the Fe II atom has a complex structure, it emits through a large number of multiplets, thus acting as one of the main coolants of the BELR (Wills et al. 1985). Secondly, studies of Fe II abundance changes in AGN over cosmic time can give important clues regarding the chemical evolution of the Universe (Hamann & Ferland 1999).

The excitation mechanisms believed to produce Fe II most efficiently are Lyα fluorescence and collisional excitation. In particular, Lyα fluorescence is the process invoked for the production of the near-IR Fe II emission lines. In the previous subsection we concluded that the theoretical predictions of Sigut & Pradhan (2003) are generally consistent with our observations, which suggests that Lyα fluorescence is indeed the dominant process. In this case then we also expect the profiles of the near-IR Fe II emission lines to be similar to those of hydrogen.

In Fig. 16 we compare the isolated profiles of the three Fe II emission lines $\lambda 9956 + 9998$ (cyan), 1.0491+1.0502 μm (blue), and 1.1126 μm (red) to those of the hydrogen emission lines Paα and Paβ (black). About half of our sources are relatively weak iron emitters and, therefore, their Fe II profiles are rather noisy. However, for the strongest iron emitters Fig. 16 clearly shows that the Fe II and hydrogen emitting regions are, as expected, cospatial. This result is similar to that obtained by Boroson & Green (1992) based on comparisons of measured Hβ widths to modeled Fe II widths. Therefore, in the absence of near-IR spectra from which to measure the widths of the resolved Fe II emission lines, one can use the widths of available hydrogen emission lines instead in order to broaden suitable Fe II templates, as is already common practice (e.g., Marziani et al. 1996).

5.4.3. Unidentified Emission Lines

For six features we could not find a suitable identification using the Fe II emission line list of Sigut & Pradhan (2003). However, comparisons of their profiles to those of the two near-IR iron emission lines Fe II 1.0491+1.0502 μm and Fe II 1.1126 μm, which are relatively strong and observed unblended, show that they are most likely so far unidentified iron emission lines. This interpretation is strengthened by the fact that the unidentified features are convincingly detected only in those eight sources that are amongst the strongest iron emitters in our sample, namely, PDS 456, 3C 273, HE 1228+013, PG 0844+349, Mrk 817, Ark 564, Mrk 79, and H 1934−063.

In Table 10 we list the rest frame wavelengths and observed fluxes of these unidentified near-IR emission lines. The given values, however, should be taken only as approximations. Although we measured the rest wavelength in that source where the feature appeared the narrowest, emission lines of AGN are often red- or blue-shifted relative to the system velocity. The measured flux, on the other hand, is overestimated, if the unidentified feature is in fact a blend of several emission lines.

In Fig. 17, left panel, we show the feature at 7161 Å. It is seen in PDS 456, but not in 3C 273, which is the only other of the above listed sources for which this spectral range is covered. The blends $\lambda 7875 + 7896$ and $\lambda 10703 + 10736$ are labeled in Figs. 14 and 3, respectively. In Fig. 17, right panel, we show the three unidentified features at 16890 Å, 16925 Å, and 17004 Å, which are most clearly observed in PDS 456, Ark 564, H 1934−063, and Mrk 79. These features are not convincingly detected in 3C 273, and the spectrum of HE 1228+013 does not cover them. We note that the features at 16925 Å and 17004 Å in PDS 456 were observed also by Simpson et al. (1999).

REFERENCES

Baldwin, J., Ferland, G., Korista, K., & Verner, D. 1995, ApJL, 455, 119

Bautista, M. A., Rudy, R. J., & Venturini, C. C. 2004, ApJ, 604, 129

Boroson, T. A., & Green, R. F. 1992, ApJS, 80, 109

Cardelli, J. A., Clayton, G. C., & Mathis, J. S. 1989, ApJ, 345, 245

Cohen, R. D. 1983, ApJ, 273, 489

Collin-Souffrin, S., & Lasota, J.-P. 1988, PASP, 100, 1041

Crenshaw, D. M., Kraemer, S. B., Bruhweiler, F. C., & Ruiz, J. R. 2001, ApJ, 555, 633

Crenshaw, D. M., et al. 2002, ApJ, 566, 187

Crenshaw, D. M., & Peterson, B. M. 1985, ApJ, 291, 677

Cushing, M. C., Vacca, W. D., & Rayner, J. T. 2004, PASP, 116, 362

Cutri, R. M., et al. 2003, The 2MASS All-Sky Catalog of Point Sources, University of Massachusetts and Infrared Processing and Analysis Center (IPAC/California Institute of Technology)

De Robertis, M. 1985, ApJ, 289, 67

Dickey, J. M., & Lockman, F. J. 1990, ARA&A, 28, 215

Elvis, M., & Karovska, M. 2002, ApJL, 581, 67

Fabricant, D., Cheimets, P., Caldwell, N., & Geary, J. 1998, PASP, 110, 79

Ferland, G. J. 2003, ARA&A, 41, 517

Ferland, G. J., Korista, K. T., Verner, D. A., Ferguson, J. W., Kingdon, J. B., & Verner, E. M. 1998, PASP, 110, 761

Gallimore, J. F., Henkel, C., Baum, S. A., Glass, I. S., Claussen, M. J., Prieto, M. A., & Von Kap-Herr, A. 2001, ApJ, 556, 694

Grandi, S. A. 1975, ApJ, 196, 465

Grandi, S. A. 1980, ApJ, 238, 10

Hamann, F., & Ferland, G. 1999, ARA&A, 37, 487

Kollatschny, W., Bischoff, K., Robinson, E. L., Welsh, W. F., & Hill, G. J. 2001, A&A, 379, 125

Marziani, P., Sulentic, J. W., Dultzin-Hacyan, D., C̃alvani, M., & Moles, M. 1996, ApJS, 104, 37

Matsuoka, Y., Oyabu, S., Tsuzuki, Y., & Kawara, K. 2007, ApJ, 663, 781

Mazzalay, X., & Rodríguez-Ardila, A. 2007, A&A, 463, 445

Morris, S. L., & Ward, M. J. 1985, MNRAS, 215, 57P

Morris, S. L., & Ward, M. J. 1988, MNRAS, 230, 639

Morris, S. L., & Ward, M. J. 1989, MNRAS, 340, 713

Netzer, H., & Davidson, K. 1979, MNRAS, 187, 871

Oliva, E., Salvati, M., Moorwood, A. F. M., & Marconi, A. 1994, A&A, 288, 457

Osterbrock, D. E., & Ferland, G. J. 2006, Astrophysics of Gaseous Nebulae and Active Galactic Nuclei (University Science Books)

Osterbrock, D. E., & Fulbright, J. P. 1996, PASP, 108, 183

Osterbrock, D. E., & Mathews, W. G. 1986, ARA&A, 24, 171

Osterbrock, D. E., Shaw, R. A., & Veilleux, S. 1990, ApJ, 352, 561

Osterbrock, D. E., & Shuder, J. M. 1982, ApJS, 49, 149

Peterson, B. M. 1993, PASP, 105, 247

Peterson, B. M., & Wandel, A. 1999, ApJL, 521, 95

Rayner, J. T., Toomey, D. W., Onaka, P. M., Denault, A. J., Stahlberger, W. E., Vacca, W. D., Cushing, M. C., & Wang, S. 2003, PASP, 115, 362

Riffel, R., Rodríguez-Ardila, A., & Pastoriza, M. G. 2006, A&A, 457, 61

Rodríguez-Ardila, A., Viegas, S. M., Pastoriza, M. G., & Prato, L. 2002a, ApJ, 565, 140

Rodríguez-Ardila, A., Viegas, S. M., Pastoriza, M. G., Prato, L., & Donzelli, C. J. 2002b, ApJ, 572, 94

Rudy, R., Erwin, P., Rossano, G. S., & Puetter, R. C. 1991, ApJ, 383, 344

Rudy, R. J., Lynch, D. K., Mazuk, S., Venturini, C. C., Puetter, R. C., & Hamann, F. 2001, PASP, 113, 916

Rudy, R. J., Mazuk, S., Puetter, R. C., & Hamann, F. 2000, ApJ, 539, 166

Rudy, R. J., Rossano, G. S., & Puetter, R. C. 1989, ApJ, 342, 235

Shang, Z., Wills, B. J., Wills, D., & Brotherton, M. S. 2007, AJ, 134, 294

Sigut, T. A. A., & Pradhan, A. K. 2003, ApJS, 145, 15

Simpson, C., Ward, M., O'Brien, P., & Reeves, J. 1999, MNRAS, 303, L23

Sulentic, J. W., Marziani, P., & Dultzin-Hacyan, D. 2000, ARA&A, 38, 521

Thompson, R. I. 1995, ApJ, 445, 700

Vacca, W. D., Cushing, M. C., & Rayner, J. T. 2003, PASP, 115, 389

Vanden Berk, D. E., et al. 2001, AJ, 122, 549

Véron, P., Gon A. C., calves, & Véron-Cetty, M.-P. 2002, A&A, 384, 826

Véron-Cetty, M.-P., Joly, M., & Véron, P. 2004, A&A, 417, 515

Véron-Cetty, M.-P., & Véron, P. 2006, A&A, 455, 773

Vestergaard, M., & Peterson, B. M. 2005, ApJ, 625, 688

Ward, M. J., Geballe, T., Smith, M., Wade, R., & Williams, P. 1987, ApJ, 316, 138

Wills, B. J., Netzer, H., & Wills, D. 1985, ApJ, 288, 94

TABLE 1

GENERAL PROPERTIES OF THE OBSERVED SAMPLE

Object Name	R.A.(J2000)	Decl.(J2000)	z	J [mag]	V [mag]	class
(1)	(2)	(3)	(4)	(5)	(6)	(7)
Mrk 335	00 06 19.52	+20 12 10.5	0.026	12.6	13.9	S1n
Mrk 590	02 14 33.56	−00 46 00.1	0.026	12.4	13.8	S1.0
Ark 120	05 16 11.42	−00 08 59.4	0.033	12.0	13.9	S1.0
Mrk 79	07 42 32.80	+49 48 34.8	0.022	12.5	14.3	S1.2
PG 0844+349	08 47 42.40	+34 45 04.0	0.064	13.4	14.5	S1.0
Mrk 110	09 25 12.87	+52 17 10.5	0.035	13.9	16.4	S1n
NGC 3227	10 23 30.58	+19 51 54.2	0.004	11.3	11.8	S1.5
NGC 4151	12 10 32.58	+39 24 20.6	0.003	10.3	11.9	S1.5
3C 273	12 29 06.70	+02 03 08.6	0.158	11.8	12.9	S1.0
HE 1228+013	12 30 50.02	+01 15 22.6	0.117	13.7	14.4	S1n
NGC 4593	12 39 39.43	−05 20 39.3	0.009	11.7	13.2	S1.0
NGC 5548	14 17 59.53	+25 08 12.4	0.017	11.8	13.7	S1.5
Mrk 817	14 36 22.07	+58 47 39.4	0.031	12.9	13.8	S1.5
Mrk 290	15 35 52.36	+57 54 09.2	0.030	13.6	15.3	S1.5
Mrk 876	16 13 57.18	+65 43 09.6	0.129	13.2	15.5	S1.0
PDS 456	17 28 19.80	−14 15 55.9	0.184	12.0	14.0	
IRAS 1750+508	17 51 16.63	+50 45 38.8	0.300	14.0	15.8	S1.2
H 1821+643	18 21 57.31	+64 20 36.4	0.297	12.8	14.2	S1.2
H 1934−063	19 37 33.01	−06 13 04.8	0.011	12.7	15.4	S1.5
Mrk 509	20 44 09.74	−10 43 24.5	0.034	12.0	13.1	S1.5
H 2106−099	21 09 09.97	−09 40 14.7	0.027	12.9	14.4	S1.2
Ark 564	22 42 39.35	+29 43 31.3	0.025	13.2	14.2	S3
NGC 7469	23 03 15.62	+08 52 26.4	0.016	11.4	13.0	S1.5

NOTE.—Columns: (1) object name; (2) and (3) position and (4) redshift from the NASA/IPAC Extragalactic Database (NED); (5) J magnitude from the Two Micron All Sky Survey (2MASS; Cutri et al. 2003); (6) V magnitude and (7) spectroscopic classification from the catalogue of Véron-Cetty & Véron (2006), where S1.0=Seyfert 1, (S1.2, S1.5)=intermediate Seyfert 1, S1n=narrow-line Seyfert 1, and S3=Seyfert 3 (LINER).

TABLE 2

IRTF Journal of Observations

Object Name	observation date	exposure [sec]	airmass	continuum S/N			telluric standard star		
				J	H	K	name	distance [deg]	airmass
(1)	(2)	(3)	(4)	(5)	(6)	(7)	(8)	(9)	(10)
Mrk 335	**2006 Jan 10**	48x120	1.422	67	132	269	HD13869	31.8	1.033
Mrk 590	**2006 Jan 09**	48x120	1.128	47	89	160	HD13936	10.2	1.333
Ark 120	**2006 Jan 08**	56x120	1.088	226	214	325	HD31411	7.3	1.204
Mrk 79	**2006 Jan 08**	56x120	1.204	68	162	338	HD45105	12.6	1.407
PG 0844+349	**2006 Jan 10**	48x120	1.266	40	83	175	HD71906	4.2	1.349
Mrk 110	**2006 Jan 09**	56x120	1.396	31	95	305	HD71906	17.8	1.192
NGC 3227	**2006 Jan 10**	16x120	1.104	57	112	240	HD89239	7.6	1.241
NGC 4151	2004 May 23	6x120	1.130	32	45	121	HD109615	4.9	1.100
	2006 Jan 08	16x120	1.067	103	212	345	HD109615	4.9	1.063
	2006 Jun 12	10x120	1.216	109	202	269	HD109615	4.9	1.263
3C 273	2004 May 23	24x120	1.054	145	248	395	HD110411	8.8	1.033
	2006 Jan 09	24x120	1.361	170	242	421	HD109309	11.6	1.354
	2006 Jun 12	24x120	1.072	163	361	478	HD109309	11.6	1.147
HE 1228+013	2006 Jan 10	16x120	1.319	12	72	209	HD109309	10.7	1.326
	2006 Jun 10	22x120	1.079	42	94	298	HD109309	10.7	1.147
NGC 4593	2004 May 23	6x120	1.473	14	42	101	HD109309	4.4	1.399
	2006 Jun 11	10x120	1.263	50	119	211	HD112304	10.8	1.240
NGC 5548	2004 May 23	18x120	1.205	19	39	80	HD127304	7.1	1.205
	2006 Jan 09	16x120	1.195	29	51	114	HD131951	14.0	1.171
	2006 Jun 12	16x120	1.103	49	110	172	HD131951	14.0	1.175
Mrk 817	2004 May 22	36x120	1.372	61	117	170	HD121409	7.8	1.552
	2006 Jun 10	32x120	1.309	39	139	231	HD121409	7.8	1.213
Mrk 290	2004 May 21	36x120	1.308	54	75	174	HD143187	2.8	1.325
	2006 Jun 11	32x120	1.301	42	148	248	HD143187	2.8	1.291
Mrk 876	**2006 Jun 10**	24x120	1.477	45	66	98	HD143187	7.1	1.416
PDS 456	2004 May 20	28x120	1.213	125	195	285	HD159415	1.8	1.233
	2006 Jun 11	24x120	1.248	194	265	452	HD155379	11.6	1.430
IRAS 1750+508	2004 May 21	24x120	1.209	50	53	112	HD153345	8.7	1.247
	2006 Jun 12	32x120	1.171	36	66	115	HD172728	13.4	1.363
H 1821+643	**2004 May 22**	24x120	1.405	62	90	147	HD172728	2.5	1.375
H 1934−063	**2006 Jun 12**	16x120	1.120	75	166	230	HD182678	8.8	1.212
Mrk 509	2004 May 20	18x120	1.194	88	213	170	HD202990	9.3	1.246
	2006 Jun 10	32x120	1.178	164	244	450	HD203893	10.7	1.212
H 2106−099	2004 May 22	18x120	1.210	73	94	156	HD202990	5.1	1.237
	2006 Jun 11	24x120	1.152	91	181	277	HD203893	6.1	1.219
Ark 564	**2006 Jun 12**	32x120	1.101	72	162	244	HD209932	17.0	1.108
NGC 7469	**2006 Jan 08**	24x120	1.808	82	149	265	HD219833	21.4	1.659

NOTE.—Columns: (1) object name; (2) observation date (bold-face indicates that the corresponding spectrum is shown in Fig. 1); (3) exposure time; (4) average airmass; S/N in the continuum over ∼ 100 Å measured at the central wavelength of the (5) J, (6) H, and (7) K band; for the telluric standard star (8) name, (9) distance from the source, and (10) average airmass.

TABLE 3

TILLINGHAST JOURNAL OF OBSERVATIONS

Object Name	IRTF observation date	observation date	exposure [sec]	airmass	cloud condition
(1)	(2)	(3)	(4)	(5)	(6)
Mrk 335	2006 Jan 10	2005 Dec 29	3x300	1.09	photom
Mrk 590	2006 Jan 09	2005 Dec 29	2x720	1.18	photom
Ark 120	2006 Jan 08	2005 Dec 29	3x480	1.18	photom
Mrk 79	2006 Jan 08	2005 Dec 29	3x720	1.06	photom
PG 0844+349	2006 Jan 10	2005 Dec 29	3x480	1.03	photom
Mrk 110	2006 Jan 09	2006 Jan 05	3x540	1.07	clear
NGC 3227	2006 Jan 10	2006 Jan 05	3x330	1.02	clear
NGC 4151	2004 May 23	2004 May 18	2x120	1.02	cirrus
	2006 Jan 08	2006 Jan 05	3x 60	1.02	clear
	2006 Jun 12	2006 Jun 19	30	1.13	photom
3C273	2006 Jan 09	2006 Jan 05	5x120	1.17	clear
	2006 Jun 12	2006 Jun 19	180	1.31	photom
HE 1228+013	2006 Jun 10	2006 Jun 20	660	1.74	photom
NGC 4593	2004 May 23	2004 May 18	2x360	1.25	cirrus
	2006 Jun 11	2006 Jun 20	600	1.74	photom
NGC 5548	2004 May 23	2004 Jul 21	2x300	1.13	cirrus
	2006 Jan 09	2006 Jan 09	3x360	1.05	clear
	2006 Jun 12	2006 Jun 20	600	1.16	photom
Mrk 817	2004 May 22	2004 Jul 21	720	1.21	cirrus
	2006 Jun 10	2006 Jul 18	1200	1.19	cloudy
Mrk 290	2004 May 21	2004 Jul 13	900	1.34	cirrus
	2006 Jun 11	2006 Jun 20	1200	1.21	cirrus
Mrk 876	2006 Jun 10	2006 Jul 21	600	1.25	cloudy
PDS 456	2006 Jun 11	2006 Jun 20	600	1.45	cirrus
IRAS 1750+508	2004 May 21	2004 Jul 12	900	1.14	cirrus
	2006 Jun 12	2006 Jun 18	900	1.23	clear
H 1821+643	2004 May 22	2004 Jul 12	720	1.24	cirrus
H 1934−063	2006 Jun 12	2006 Jul 22	3x300	1.33	cloudy
Mrk 509	2004 May 20	2004 Jul 12	2x240	1.35	cirrus
	2006 Jun 10	2006 Jun 05	2x300	1.36	cloudy
H 2106−099	2004 May 22	2004 Jul 12	2x420	1.33	cirrus
	2006 Jun 11	2006 Jun 05	2x480	1.35	cirrus
Ark 564	2006 Jun 12	2006 Jul 21	600	1.00	cloudy
NGC 7469	2006 Jan 08	2005 Dec 29	3x210	1.30	photom

NOTE.—Columns: (1) object name; (2) IRTF observation date (reproduced from Table 2); (3) Tillinghast UT observation date; (4) exposure time; (5) airmass; and (6) cloud condition.

TABLE 4

OSBERVED NEAR-INFRARED EMISSION LINES

Element	vacuum wavelength [Å]	transition type	term	Fe II multiplets wavelength [Å]	term
(1)	(2)	(3)	(4)	(5)	(6)
He I	7067.2	E1	^{3}P^o-^{3}S		
[O II]	7320.9	E2	^{2}D^o-^{2}P^o		
				7462.4	b^{4}D-z^{4}D
				7711.7	b^{4}D-z^{4}D
O I	7776.3	E1	^{5}S^o-^{5}P		
[Fe XI]	7894.0	M1	^{3}P-^{3}P		
				8157.5	b^{6}D-v^{4}F
				8190.6	b^{6}D-x^{6}F
				8228.9	b^{6}D-v^{4}F
				8287.5	b^{6}D-x^{6}F
				8357.2	b^{6}D-x^{6}F
O I	8448.7	E1	^{3}S^o-^{3}P		
Ca II	8500.4	E1	^{2}D-^{2}P^o		
Ca II	8544.4	E1	^{2}D-^{2}P^o		
Pa14	8600.8	E1	3-14		
[Fe II]	8619.3	E2	a^{4}F-a^{4}P		
Ca II	8664.5	E1	^{2}D-^{2}P^o		
Pa13	8667.4	E1	3-13		
Pa12	8752.9	E1	3-12		
Pa11	8865.2	E1	3-11		
				8926.6	d^{4}D-u^{4}D
Pa10	9017.4	E1	3-10		
[S III]	9071.1	M1	^{3}P-^{1}D		
				9122.9	d^{4}D-u^{4}D
				9132.4	d^{4}D-v^{4}F
				9175.9	d^{4}D-v^{4}F
				9178.1	d^{4}D-v^{4}F
				9196.9	d^{4}D-u^{4}D
				9203.1	d^{4}D-v^{4}F
[Fe II]	9229.1	E2	a^{4}F-a^{4}P		
Pa9	9231.5	E1	3-9		
				9406.7	d^{4}D-x^{6}F
[S III]	9533.2	M1	^{3}P-^{1}D		
Paϵ	9548.6	E1	3-8		
				9572.6	z^{4}P-d^{4}P
				9812.0	z^{4}P-d^{4}P
[C I]	9826.8	M1	^{3}P-^{1}D		
[C I]	9853.0	M1	^{3}P-^{1}D		
[S VIII]	9913.8	M1	^{2}P^o-^{2}P^o		
				9956.3	z^{4}F-b^{4}G
				9997.6	z^{4}F-b^{4}G
Paδ	10052.1	E1	3-7		
He II	10126.4	E1	4-5		
				10131.8	z^{4}P-d^{4}P
				10173.5	z^{4}D-b^{4}G
[S II]	10289.6	M1	^{2}D^o-^{2}P^o		
[S II]	10323.3	M1	^{2}D^o-^{2}P^o		

20

TABLE 4—*Continued*

Element	vacuum wavelength [Å]	transition type	term	Fe II multiplets wavelength [Å]	term
(1)	(2)	(3)	(4)	(5)	(6)
[S II]	10339.2	M1	^{2}D^o-^{2}P^o		
[S II]	10373.3	E2	^{2}D^o-^{2}P^o		
[N I]	10400.6	M1	^{2}D^o-^{2}P^o		
[N I]	10410.2	M1	^{2}D^o-^{2}P^o		
				10491.0	z^{4}F-b^{4}G
				10501.5	z^{4}F-b^{4}G
He I	10833.2	E1	^{3}S-^{3}P^o		
				10862.6	z^{4}F-b^{4}G
Paγ	10941.1	E1	3-6		
				11125.6	z^{4}F-b^{4}G
O I	11290.0	E1	^{3}P-^{3}D^o		
[P II]	11471.3	M1	^{3}P-^{1}D		
He II	11629.6	E1	5-7		
[P II]	11886.1	M1	^{3}P-^{1}D		
[S IX]	12523.	M1	^{3}P-^{3}P		
[Fe II]	12570.2	M1	a^{6}D-a^{4}D		
[Fe II]	12791.3	M1	a^{6}D-a^{4}D		
Paβ	12821.6	E1	3-5		
O I	13168.5	E1	^{3}P-^{3}S^o		
[Fe II]	13209.2	M1	a^{6}D-a^{4}D		
[Si X]	14304.9	M1	^{2}P^o-^{2}P^o		
[Fe II]	15338.9	E2	a^{4}F-a^{4}D		
[Fe II]	16440.0	M1	a^{4}F-a^{4}D		
[Fe II]	16773.3	M1	a^{4}F-a^{4}D		
Br11	16811.1	E1	4-11		
Br10	17366.9	E1	4-10		
Brϵ	18179.1	E1	4-9		
Paα	18756.1	E1	3-4		
Brδ	19450.9	E1	4-8		
H$_2$	19570.				
[Si VI]	19650.	M1	^{2}P^o-^{2}P^o		
H$_2$	20332.				
H$_2$	21213.				
Brγ	21661.2	E1	4-7		
H$_2$	22230.				
H$_2$	22470.				
[Ca VIII]	23211.	M1	^{2}P^o-^{2}P^o		

NOTE.—Columns: (1) ion; (2) vacuum rest wavelength; (3) transition type, where E1=allowed transition, M1=magnetic dipole forbidden transition, and E2=electric quadrupole forbidden transition; (4) transition term; (5) wavelength and (6) transition term of neighboring Fe II multiplets.

TABLE 5

EMISSION LINE MEASUREMENTS

Object Name	continuum flux [erg/s/cm^2/Å]	broad component			narrow component		
		flux [erg/s/cm^2]	FWHM [km/s]	Δ v [km/s]	type	flux [erg/s/cm^2]	FWHM [km/s]
(1)	(2)	(3)	(4)	(5)	(6)	(7)	(8)
Paα							
PDS 456	4.73e−15	4.32e−13	2022				
3C 273	6.76e−15	7.66e−13	2946	+ 328	e	3.68e−14	762
Mrk 876	1.03e−15	1.21e−13	5505		i	8.08e−15	475
HE 1228+013	9.81e−16	6.86e−14	1957		e	1.38e−14	560
PG 0844+349	8.44e−16	1.12e−13	2219	+ 402			
Mrk 110	1.07e−15	1.83e−13	1827		e	1.96e−14	447
Mrk 509	3.18e−15	6.07e−13	3068		e	4.81e−14	578
Ark 120	6.76e−15	6.40e−13	5085	+ 435			
Mrk 817	1.66e−15	1.28e−13	4665		i	5.43e−15	323
Mrk 290	1.16e−15	1.51e−13	3542		i	1.22e−14	291
H 2106−099	1.50e−15	2.16e−13	1769		e	1.48e−14	587
Mrk 335	1.74e−15	1.29e−13	1642	− 381	e	4.42e−14	600
Mrk 590	8.19e−16	2.60e−14	4727	−1433			
Ark 564	1.10e−15	1.02e−13	854		e	1.00e−14	402
Mrk 79	2.53e−15	2.38e−13	3401		i	3.00e−14	726
NGC 5548	1.92e−15	>1.51e−13	4555		i	2.18e−14	477
NGC 7469	4.09e−15	1.60e−13	1160		i	2.31e−14	349
H 1934−063	2.19e−15	>1.63e−13	1412		e	6.50e−14	474
NGC 4593	3.31e−15				i	9.30e−15	229
Paβ							
IRAS 1750+508	3.45e−16	4.14e−14	1993	+ 363			
H 1821+643	1.40e−15	1.77e−13	5231	+1366	i	1.30e−15	323
PDS 456	4.19e−15	3.49e−13	2068				
3C 273	7.36e−15	6.39e−13	2916	+ 410	e	2.36e−14	762
Mrk 876	1.11e−15	7.18e−14	6020		i	2.44e−15	407
HE 1228+013	1.01e−15	6.09e−14	1964		e	1.00e−14	560
PG 0844+349	1.35e−15	9.76e−14	2410	+ 353			
Mrk 110	1.24e−15	1.38e−13	1918		e	1.02e−14	447
Mrk 509	3.78e−15	4.78e−13	3077		e	2.43e−14	578
Ark 120	7.44e−15	5.42e−13	5114				
Mrk 817	1.92e−15	1.28e−13	5530		i	1.21e−15	288
Mrk 290	1.35e−15	1.43e−13	4242		i	7.30e−15	428
H 2106−099	1.75e−15	1.57e−13	2422		e	1.29e−14	587
Mrk 335	1.94e−15	1.54e−13	1858	− 346	e	2.96e−14	600
Mrk 590	1.33e−15	1.35e−14	3964	− 735			
Ark 564	1.25e−15	6.62e−14	1616		e	2.95e−14	402
Mrk 79	2.06e−15	1.71e−13	3523		i	7.24e−15	407
NGC 5548	2.21e−15	1.63e−13	6525	−1369	i	9.19e−15	438

22

TABLE 5—*Continued*

Object Name	continuum flux [erg/s/cm²/Å]	broad component			narrow component		
		flux [erg/s/cm²]	FWHM [km/s]	Δ v [km/s]	type	flux [erg/s/cm²]	FWHM [km/s]
(1)	(2)	(3)	(4)	(5)	(6)	(7)	(8)
NGC 7469	4.88e−15	1.59e−13	1792		i	3.37e−14	377
H 1934−063	2.85e−15	1.26e−13	1441		e	4.00e−14	474
NGC 4593	3.22e−15	2.64e−13	3791		i	2.11e−15	325
NGC 3227	9.15e−15	3.20e−13	2955		i	2.67e−14	428
NGC 4151	8.74e−15	1.12e−12	4667	+ 821	i	1.24e−13	468
Paγ							
IRAS 1750+508	4.07e−16	2.50e−14	2710				
H 1821+643	1.45e−15	9.69e−14		+1903			
PDS 456	4.51e−15	2.33e−13					
3C 273	7.93e−15	3.78e−13	3116	+ 389	e	9.81e−15	762
Mrk 876	1.16e−15	9.31e−14					
HE 1228+013	1.07e−15	6.15e−14	2235		e	4.51e−15	560
PG 0844+349	1.58e−15	5.59e−14	2499				
Mrk 110	1.17e−15	9.03e−14	2231		e	4.80e−15	447
Mrk 509	4.14e−15	3.14e−13	3390		e	1.02e−14	578
Ark 120	7.79e−15	4.91e−13					
Mrk 817	2.02e−15	1.03e−13					
Mrk 290	1.41e−15	1.14e−13			i	4.44e−15	513
H 2106−099	1.87e−15	1.07e−13	2541		e	5.87e−15	587
Mrk 335	2.11e−15	8.24e−14	1917	− 420	e	1.51e−14	600
Mrk 590	1.46e−15	3.30e−14	3295	−1135			
Ark 564	1.43e−15	3.98e−14	1537		e	1.64e−14	402
Mrk 79	2.00e−15	1.26e−13			i	2.99e−15	381
NGC 5548	2.32e−15	1.26e−13		−1174	i	3.75e−15	378
NGC 7469	4.82e−15	8.26e−14	1793		i	1.86e−14	400
H 1934−063	3.20e−15	6.51e−14	1447		e	2.40e−14	474
NGC 4593	3.12e−15	1.60e−13					
NGC 3227	9.77e−15	1.47e−13					
NGC 4151	9.23e−15	8.26e−13		+ 847	i	8.80e−14	579
Paδ							
IRAS 1750+508	4.45e−16	1.93e−14	2083	+ 400			
H 1821+643	1.63e−15	8.83e−14	4916	+1236			
PDS 456	4.52e−15	1.53e−13	2077				
3C 273	8.52e−15	2.89e−13	3079	+ 427	e	1.20e−14	762
Mrk 876	1.23e−15	4.13e−14	5805				
HE 1228+013	1.14e−15	2.90e−14	1923		e	4.19e−15	560
PG 0844+349	1.77e−15	4.45e−14	2403	+ 346			

TABLE 5—*Continued*

Object Name	continuum flux [erg/s/cm^2/Å]	broad component flux [erg/s/cm^2]	FWHM [km/s]	Δ v [km/s]	narrow component type	flux [erg/s/cm^2]	FWHM [km/s]
(1)	(2)	(3)	(4)	(5)	(6)	(7)	(8)
Mrk 110	1.45e−15	6.50e−14	1978				
Mrk 509	4.49e−15	2.06e−13	3157		e	1.15e−14	578
Ark 120	8.21e−15	3.39e−13	5062				
Mrk 817	2.11e−15	9.17e−14	5280				
Mrk 290	1.45e−15	7.31e−14	4203		i	2.83e−15	618
H 2106−099	1.99e−15	8.21e−14	2263		e	5.48e−15	587
Mrk 335	2.28e−15	8.41e−14	2117		e	1.16e−14	600
Mrk 590	1.59e−15	5.64e−15	3991	− 725			
Ark 564	1.57e−15	3.46e−14	1831		e	9.12e−15	402
Mrk 79	2.03e−15	8.93e−14	3527		i	1.57e−15	346
NGC 5548	2.31e−15	8.85e−14	9822	− 833	i	3.15e−15	454
NGC 7469	4.90e−15	7.02e−14	1974		i	7.19e−15	394
H 1934−063	3.46e−15	6.43e−14	1474		e	1.65e−14	474
NGC 4593	3.05e−15	1.74e−13	3698				
NGC 3227	1.02e−14	2.10e−13	2946		i	5.04e−15	409
NGC 4151	9.35e−15	5.05e−13	5639	+ 385	i	3.93e−14	486

Paε

IRAS 1750+508	4.81e−16	1.22e−14	2017	+ 412			
H 1821+643	1.83e−15	4.06e−14	5262	+1442			
PDS 456	4.90e−15	9.17e−14	2490				
3C 273	9.21e−15	1.46e−13	3131	+ 415	e	9.10e−15	762
Mrk 876	1.25e−15	2.11e−14	6176				
HE 1228+013	1.20e−15	3.27e−14	2191				
PG 0844+349	1.95e−15	2.52e−14	1774				
Mrk 110	1.50e−15	4.85e−14	2116		e	2.86e−15	447
Mrk 509	4.82e−15	1.25e−13	2983		e	8.33e−15	578
Ark 120	8.71e−15	1.18e−13	5262	+ 383			
Mrk 817	2.29e−15	2.53e−14	5543		i	8.11e−16	317
Mrk 290	1.52e−15	4.01e−14	4496		i	1.44e−15	424
H 2106−099	2.08e−15	4.93e−14	2824		e	4.22e−15	587
Mrk 335	2.40e−15	4.43e−14	2052	− 452	e	7.66e−15	600
Mrk 590	1.57e−15	8.23e−15	5368				
Ark 564	1.70e−15	1.67e−14	1601		e	6.71e−15	402
Mrk 79	2.09e−15	5.87e−14	3384		i	2.55e−15	415
NGC 5548	2.32e−15	2.15e−14	5933	−1005	i	9.46e−16	144
NGC 7469	4.72e−15	8.19e−14	2681		i	1.77e−15	210
H 1934−063	3.64e−15	5.25e−14	2062		e	1.61e−14	474
NGC 4593	3.03e−15	1.01e−13	5350				
NGC 3227	9.87e−15	1.56e−13	3922				
NGC 4151	9.58e−15	2.04e−13	4544	+ 770			

TABLE 5—*Continued*

Object Name	continuum flux [erg/s/cm²/Å]	broad component			narrow component		
		flux [erg/s/cm²]	FWHM [km/s]	Δ v [km/s]	type	flux [erg/s/cm²]	FWHM [km/s]
(1)	(2)	(3)	(4)	(5)	(6)	(7)	(8)
Brγ							
HE 1228+013	9.39e−16				e	1.17e−15	560
PG 0844+349	6.95e−16	1.58e−14	2205	+ 321			
Mrk 110	1.02e−15	2.50e−14	1933		e	1.75e−15	447
Mrk 509	2.83e−15	7.25e−14	3096		e	4.02e−15	578
Ark 120	5.93e−15	8.18e−14	5455	+ 639			
Mrk 817	1.55e−15	2.58e−14	6623	− 431	i	7.36e−16	558
Mrk 290	1.06e−15	2.39e−14	4364		i	1.10e−15	486
H 2106−099	1.40e−15	2.73e−14	2290		e	1.47e−15	587
Mrk 335	1.84e−15	3.09e−14	2043	− 357	e	4.37e−15	600
Mrk 590	6.16e−16	2.17e−15	5205	−1140			
Ark 564	1.07e−15	7.33e−15	1665		e	5.27e−15	402
Mrk 79	2.38e−15	3.21e−14	4191		i	2.16e−15	432
NGC 5548	1.65e−15	2.18e−14	10278		i	2.25e−15	608
NGC 7469	3.82e−15	2.69e−14	2437		i	9.92e−15	415
H 1934−063	1.93e−15	1.70e−14	1404		e	6.64e−15	474
NGC 4593	3.22e−15	7.09e−14	4674				
NGC 3227	4.96e−15	8.61e−14	3625		i	6.66e−15	382
NGC 4151	7.66e−15	1.54e−13	4988	+ 632	i	2.53e−14	442
Hα							
IRAS 1750+508	1.11e−15	4.82e−13	2346	+ 370			
H 1821+643	3.85e−15	1.93e−12	5062	+1165	i	1.29e−14	420
Mrk 876	2.62e−15				i	9.63e−15	389
HE 1228+013	2.84e−15	>4.85e−13	1886		e	8.16e−14	560
PG 0844+349	5.52e−15	1.22e−12	2018				
Mrk 110	2.86e−15	1.48e−12	1982		e	1.46e−13	447
Mrk 509	8.94e−15	4.74e−12	3259		e	3.94e−13	578
Ark 120	1.68e−14	7.23e−12	4812	+ 279			
Mrk 817	3.66e−15	1.22e−12	5013		i	2.35e−14	466
Mrk 290	1.41e−15	5.39e−13	4274		i	6.77e−14	512
H 2106−099	4.67e−15	1.61e−12	2391		e	1.51e−13	587
Mrk 335	6.68e−15	2.37e−12	1848	− 279	e	3.40e−13	600
Mrk 590	4.93e−15	3.49e−13	4409	− 553	i	3.38e−14	503
Ark 564	3.06e−15	5.80e−13	1649		e	2.38e−13	402
Mrk 79	4.39e−15	1.94e−12	3935		i	2.29e−13	553
NGC 5548	4.33e−15	1.12e−12	5850	− 736	i	1.11e−13	375
NGC 7469	1.35e−14	2.66e−12	2458		i	8.65e−13	297
H 1934−063	6.96e−15	1.21e−12	1518		e	4.22e−13	474

25

TABLE 5—*Continued*

Object Name	continuum flux [erg/s/cm²/Å]	broad component			narrow component		
		flux [erg/s/cm²]	FWHM [km/s]	Δ v [km/s]	type	flux [erg/s/cm²]	FWHM [km/s]
(1)	(2)	(3)	(4)	(5)	(6)	(7)	(8)
NGC 4593	8.28e−15	2.06e−12	3738		i	1.25e−13	585
NGC 3227	1.31e−14	2.41e−12	3430		i	4.70e−13	571
NGC 4151	2.98e−14	1.42e−11	5259	+ 567	i	3.64e−12	475

<div align="center">Hβ</div>

Object Name	continuum flux	broad flux	FWHM	Δ v	type	narrow flux	FWHM
IRAS 1750+508	1.93e−15	2.00e−13	2572				
H 1821+643	5.53e−15	5.17e−13	6623	+2073	i	4.19e−15	358
PDS 456	1.20e−14	9.47e−13	3176	− 475			
3C 273	2.42e−14	2.22e−12	3957	+ 278	e	4.76e−14	762
Mrk 876	3.43e−15	3.34e−13	8368	+ 358	i	2.45e−15	716
HE 1228+013	3.87e−15	2.48e−13	2177		e	1.56e−14	560
PG 0844+349	8.68e−15	6.15e−13	2312				
Mrk 110	3.45e−15	5.22e−13	2306		e	2.91e−14	447
Mrk 509	1.13e−14	1.69e−12	3961		e	1.07e−13	578
Ark 120	2.62e−14	3.92e−12	5936	+ 284			
Mrk 817	5.17e−15	5.03e−13	6740	− 660	i	6.84e−15	543
Mrk 290	1.69e−15	2.56e−13	5077		i	1.75e−14	518
H 2106−099	4.96e−15	6.25e−13	2909	− 333	e	2.49e−14	587
Mrk 335	9.78e−15	1.15e−12	2446	− 315	e	1.02e−13	600
Mrk 590	4.42e−15	3.06e−13	9880	−1203	i	1.39e−15	185
Ark 564	4.29e−15	3.07e−13	1388		e	4.15e−14	402
Mrk 79	5.57e−15	8.57e−13	3694		i	3.27e−14	383
NGC 5548	4.95e−15	3.92e−13	10005		i	4.66e−14	580
NGC 7469	1.69e−14	1.80e−12	1980		i	1.10e−13	308
H 1934−063	8.09e−15	3.93e−13	1715		e	7.57e−14	474
NGC 4593	9.08e−15	1.17e−12	4354		i	8.97e−15	284
NGC 3227	1.06e−14	9.79e−13	3953		i	4.25e−14	494
NGC 4151	3.24e−14	5.79e−12	4870	+ 605	i	9.19e−13	518

<div align="center">Hγ</div>

Object Name	continuum flux	broad flux	FWHM	Δ v	type	narrow flux	FWHM
IRAS 1750+508	2.47e−15	8.17e−14	2687				
H 1821+643	6.86e−15	1.54e−13	5453	+1465	i	1.52e−15	470
PDS 456	1.42e−14	2.17e−13					
3C 273	2.97e−14	5.76e−13	3252		e	1.69e−14	762
Mrk 876	4.20e−15	8.41e−14	6449		i	2.74e−15	608
HE 1228+013	5.17e−15	7.10e−14	1665		e	4.12e−15	560
PG 0844+349	9.92e−15	2.08e−13	2472				
Mrk 110	3.94e−15	1.77e−13	2684	+ 422	e	9.50e−15	447
Mrk 509	1.32e−14	4.43e−13	3220		e	4.03e−14	578

TABLE 5—*Continued*

Object Name	continuum flux [erg/s/cm²/Å]	broad component flux [erg/s/cm²]	broad component FWHM [km/s]	Δ v [km/s]	narrow component type	narrow component flux [erg/s/cm²]	narrow component FWHM [km/s]
(1)	(2)	(3)	(4)	(5)	(6)	(7)	(8)
Ark 120	3.46e−14	7.90e−13	5402	+ 449			
Mrk 817	6.58e−15	1.11e−13			i	1.05e−15	387
Mrk 290	1.90e−15	5.35e−14	4336		i	5.86e−15	546
H 2106−099	5.27e−15	1.65e−13	2787		e	1.68e−14	587
Mrk 335	1.13e−14	2.94e−13	1992	− 366	e	3.66e−14	600
Mrk 590	3.45e−15	4.26e−14	3983	− 719			
Ark 564	4.55e−15	5.65e−14	1216		e	1.15e−14	402
Mrk 79	6.05e−15	1.80e−13			i	1.51e−14	442
NGC 5548	4.90e−15	1.18e−13	6920	−1334	i	8.07e−15	415
NGC 7469	1.83e−14	3.35e−13	1934		i	4.00e−14	352
H 1934−063	8.91e−15	1.10e−13	1444		e	2.13e−14	474
NGC 4593	9.56e−15	2.64e−13					
NGC 3227	9.79e−15	1.57e−13	3769	+ 325	i	9.30e−15	504
NGC 4151	3.44e−14	1.71e−12	4234	+ 594	i	3.55e−13	518
He I λ5876							
3C 273	1.54e−14	1.53e−13	4871	+ 572	i	4.16e−15	336
Mrk 876	2.35e−15	1.78e−14	3811	− 653	i	9.96e−16	393
HE 1228+013	2.47e−15	3.14e−15	3982	+ 347	i	1.22e−15	378
PG 0844+349	6.61e−15	7.08e−14	1884				
Mrk 110	2.96e−15	8.51e−14	2906	+ 388	e	3.40e−15	447
Mrk 509	9.33e−15	2.68e−13	4257		e	1.20e−14	578
Ark 120	2.00e−14	3.90e−13	7166	+ 444	i	1.40e−14	822
Mrk 817	3.92e−15	6.55e−14	6914		i	2.42e−15	536
Mrk 290	1.58e−15	3.03e−14	6326	+ 403	i	2.14e−15	510
H 2106−099	4.85e−15	8.59e−14	4792		i	1.69e−14	1047
Mrk 335	7.79e−15	1.29e−13	5395		i	4.00e−14	1042
Ark 564	3.78e−15	1.83e−14	3489		i	8.90e−15	521
Mrk 79	4.92e−15	1.14e−13	3597		i	6.22e−15	388
NGC 5548	4.96e−15	3.38e−14	9530	−2904	i	4.24e−15	419
NGC 7469	1.56e−14	2.42e−13	4420	+ 388	i	4.54e−14	587
H 1934−063	7.35e−15	2.84e−14	1820	+ 332	e	1.46e−14	474
NGC 4593	9.23e−15	2.09e−13	5539	− 311	i	4.50e−15	383
NGC 3227	1.29e−14	2.12e−13	5083		i	1.05e−14	475
NGC 4151	3.06e−14	7.16e−13	9985	− 791	i	1.04e−13	475
He I 1.0830 μm							
IRAS 1750+508	4.14e−16	8.64e−14	1800				
H 1821+643	1.46e−15	2.63e−13	4877	+ 831	i	1.45e−14	540

TABLE 5—*Continued*

Object Name	continuum flux [erg/s/cm^2/Å]	broad component			narrow component		
		flux [erg/s/cm^2]	FWHM [km/s]	Δ v [km/s]	type	flux [erg/s/cm^2]	FWHM [km/s]
(1)	(2)	(3)	(4)	(5)	(6)	(7)	(8)
PDS 456	4.50e−15	1.30e−13					
3C 273	8.00e−15	7.76e−13	3200		e	3.81e−14	762
Mrk 876	1.17e−15	1.70e−13	5643	− 859	i	1.73e−14	1094
HE 1228+013	1.09e−15	3.84e−14	1858		e	6.02e−15	560
PG 0844+349	1.60e−15	8.94e−14	2176		e	8.12e−15	467
Mrk 110	1.33e−15	2.77e−13	2001		e	4.35e−14	447
Mrk 509	4.18e−15	1.10e−12	2986		e	8.06e−14	578
Ark 120	7.84e−15	9.13e−13	4506		i	5.71e−14	728
Mrk 817	2.03e−15	2.28e−13	4274		i	2.26e−14	543
Mrk 290	1.41e−15	1.76e−13	3107		i	6.07e−14	501
H 2106−099	1.89e−15	2.81e−13	2615		e	6.04e−14	587
Mrk 335	2.13e−15	2.66e−13	2026		e	5.86e−14	600
Mrk 590	1.48e−15	4.84e−14	3393	− 789	i	8.29e−15	474
Ark 564	1.45e−15	6.99e−14	1641		e	3.44e−14	402
Mrk 79	2.00e−15	3.10e−13	2512		i	4.35e−14	418
NGC 5548	2.33e−15	2.11e−13	6087	−1346	i	1.17e−13	645
NGC 7469	4.86e−15	3.71e−13	2012		i	6.46e−14	407
H 1934−063	3.24e−15	1.73e−13	1578		e	7.93e−14	474
NGC 4593	3.13e−15	5.40e−13	3257		i	5.54e−14	474
NGC 3227	9.87e−15	7.30e−13	3034	+ 432	i	1.85e−13	653
NGC 4151	9.29e−15	1.95e−12	2972		i	7.69e−13	424
O I λ8446							
IRAS 1750+508	6.39e−16	1.47e−14	1734	+ 497			
H 1821+643	2.31e−15	8.00e−14	5117	+1431			
PDS 456	6.09e−15	1.86e−13	2088				
3C 273	1.19e−14	2.43e−13	2656	+ 391	e	1.33e−14	762
Mrk 876	1.60e−15	4.72e−14	4655				
HE 1228+013	1.57e−15	3.79e−14	1597		e	3.64e−15	560
PG 0844+349	2.57e−15	3.72e−14	1603	+ 430			
Mrk 110	1.92e−15	5.42e−14	2270		e	3.33e−15	447
Mrk 509	6.74e−15	2.42e−13	3282		e	9.63e−15	578
Ark 120	1.10e−14	3.23e−13	4468				
Mrk 817	2.82e−15	8.98e−14	5258	− 362			
Mrk 290	1.89e−15	6.13e−14	4593	+ 327			
H 2106−099	2.73e−15	6.57e−14	2330		e	4.86e−15	587
Mrk 335	3.29e−15	6.38e−14	1685	− 337	e	1.43e−14	600
Mrk 590	1.66e−15	8.58e−15	4420	− 682			
Ark 564	2.22e−15	4.10e−14	1557		e	2.24e−14	402
Mrk 79	2.53e−15	8.18e−14	3326				
NGC 5548	2.64e−15	6.40e−14	5909	−1285			

Table 5—*Continued*

Object Name	continuum flux [erg/s/cm^2/Å]	broad component			narrow component		
		flux [erg/s/cm^2]	FWHM [km/s]	Δ v [km/s]	type	flux [erg/s/cm^2]	FWHM [km/s]
(1)	(2)	(3)	(4)	(5)	(6)	(7)	(8)
NGC 7469	5.22e−15	8.03e−14	1504	+ 330			
H 1934−063	4.47e−15	1.02e−13	1395		e	2.57e−14	474
NGC 4593	3.71e−15	1.43e−13	3358				
NGC 3227	1.09e−14	1.50e−13	3631				
NGC 4151	1.18e−14	3.43e−13	4228	+ 856			
O I 1.1287 μm							
IRAS 1750+508	3.87e−16	8.27e−15	1684	+ 524			
H 1821+643	1.45e−15	4.83e−14	5852				
PDS 456	4.53e−15	2.63e−14	1323				
3C 273	7.70e−15	1.38e−13	2582	+ 420	e	3.91e−15	762
Mrk 876	1.13e−15	1.69e−14	3013				
HE 1228+013	1.04e−15	2.37e−14	1808		e	3.42e−15	560
PG 0844+349	1.50e−15	2.24e−14	1853	+ 324			
Mrk 110	1.29e−15	2.15e−14	1628		e	1.89e−15	447
Mrk 509	4.00e−15	9.35e−14	2911		e	3.40e−15	578
Ark 120	7.63e−15	9.96e−14	4333				
Mrk 817	1.99e−15	3.15e−14	4662				
Mrk 290	1.39e−15	2.21e−14	4691				
H 2106−099	1.82e−15	3.22e−14	2459		e	2.32e−15	587
Mrk 335	2.04e−15	2.91e−14	1957		e	8.33e−15	600
Mrk 590	1.40e−15	7.25e−15	4846				
Ark 564	1.38e−15	2.23e−14	1349		e	1.32e−14	402
Mrk 79	1.99e−15	3.55e−14	3428				
NGC 5548	2.30e−15	1.77e−14	6359	−2017			
NGC 7469	4.71e−15	3.66e−14	1550				
H 1934−063	3.09e−15	5.36e−14	1405		e	1.58e−14	474
NGC 4593	3.10e−15	6.11e−14	3256				
NGC 3227	9.42e−15	8.84e−14	3248	+ 446			
NGC 4151	9.01e−15	1.17e−13	3466	+1044			

NOTE.—Columns: (1) object name; (2) continuum flux at the line's vacuum rest wavelength; (3) flux and (4) FWHM of the broad component (uncorrected for instrumental broadening). Note that the latter is omitted if the line was measured using the Paα or Paβ template.; (5) shift of the broad component's center relative to the expected vacuum rest wavelength. Note that we give only shifts corresponding to more than two pixels on the detector (for SpeX spectra > 320 km s^{-1} and for FAST spectra > 270 km s^{-1}).; (6) type of subtracted narrow component, where i: inflected, and e: estimated (see Section 4.3); (7) flux and (8) FWHM (uncorrected for instrumental broadening) of the narrow component.

TABLE 6

IRON EMISSION LINES

| Object Name | Fe II $\lambda4440-4700$ | | Fe II $\lambda8150-8365$ | | Fe II $\lambda9407$ | | Fe II $\lambda9573$ | | Fe II $\lambda9812$ | | Fe II $\lambda9956+9998$ | |
| | flux [erg/s/cm^2] | ratio* (10.96**) | flux [erg/s/cm^2] | ratio* (1.28) | flux [erg/s/cm^2] | ratio* (0.40) | flux [erg/s/cm^2] | ratio* (0.29) | flux [erg/s/cm^2] | ratio* (0.12) | flux [erg/s/cm^2] | ratio* (0.88) |
(1)	(2)	(3)	(4)	(5)	(6)	(7)	(8)	(9)	(10)	(11)	(12)	(13)
IRAS 1750+508	7.48e−14	7.48	5.75e−15	0.58			1.60e−16	0.02			3.61e−15	0.36
PDS 456	6.09e−13	13.36	4.94e−14	1.08	1.14e−14	0.25	6.83e−15	0.15			5.63e−14	1.23
3C 273	7.10e−13	16.95	9.73e−14	2.32							5.38e−14	1.28
Mrk 876	1.37e−13	21.61	1.03e−14	1.62							7.97e−15	1.26
HE 1228+013	3.32e−13	19.53	1.96e−14	1.15	6.05e−15	0.36			3.16e−15	0.19	1.99e−14	1.17
PG 0844+349	4.76e−13	39.34	2.31e−14	1.91	6.04e−15	0.50					1.45e−14	1.20
Mrk 110	6.88e−14	22.12	2.32e−14	7.46							4.86e−15	1.56
Mrk 509	2.18e−13	6.23	8.27e−14	2.36			2.54e−15	0.07			5.12e−14	1.46
Ark 120	2.08e−12	34.84	1.25e−13	2.09							4.35e−14	0.73
Mrk 817	2.81e−13	40.49	2.17e−14	3.13			1.07e−15	0.15			6.64e−15	0.96
Mrk 290	8.66e−14	44.64	2.21e−14	11.39							1.11e−14	5.72
H 2106−099	3.37e−13	20.42	3.74e−14	2.27			5.12e−15	0.31			2.85e−14	1.73
Mrk 335	4.24e−13	22.32	6.02e−14	3.17	7.71e−16	0.04	6.75e−15	0.36	2.04e−15	0.11	2.22e−14	1.17
Mrk 590	1.84e−13	31.24	2.33e−14	3.96	2.52e−15	0.43					1.64e−15	0.28
Ark 564	2.39e−13	16.71	3.49e−14	2.44	7.52e−15	0.53	2.67e−15	0.19	5.57e−16	0.04	1.78e−14	1.24
Mrk 79	2.38e−13	40.75	3.79e−14	6.49	6.89e−15	1.18			6.54e−15	1.12	1.49e−14	2.55
NGC 7469	6.93e−13	78.04	3.90e−14	4.39	3.53e−15	0.40					2.67e−14	3.01
H 1934−063	3.84e−13	16.41	5.44e−14	2.32	1.15e−14	0.49	9.07e−16	0.04	1.86e−15	0.08	4.53e−14	1.94
NGC 4593	7.04e−13	64.00	5.08e−14	4.62	2.56e−15	0.23	2.52e−15	0.23			2.47e−14	2.25
NGC 3227	4.12e−13	22.64	3.76e−14	2.07							3.86e−14	2.12
NGC 4151	2.57e−13	66.41	2.57e−14	6.64					2.21e−15	0.57	3.78e−14	9.77

TABLE 6—*Continued*

Object Name	Fe II 1.0132+1.0174 μm flux [erg/s/cm²]	ratio* (0.30)	Fe II 1.0174 μm flux [erg/s/cm²]	ratio* (0.09)	Fe II 1.0491+1.0502 μm flux [erg/s/cm²]	ratio* (1.00)	Fe II 1.0863 μm flux [erg/s/cm²]	ratio* (0.56)	Fe II 1.1126 μm flux [erg/s/cm²]	ratio* (0.30)	FWHM [km/s]
(1)	(14)	(15)	(16)	(17)	(18)	(19)	(20)	(21)	(22)	(23)	(24)
IRAS 1750+508					1.00e−14	1.00			2.86e−15	0.29	2335
PDS 456	1.15e−14	0.25			4.56e−14	1.00	2.05e−14	0.45	1.02e−14	0.22	1841
3C 273	1.66e−14	0.40			4.19e−14	1.00			1.54e−14	0.37	2085
Mrk 876	2.31e−15	0.36			6.34e−15	1.00					4813
HE 1228+013	6.27e−15	0.37			1.70e−14	1.00	6.84e−15	0.40	1.16e−14	0.68	1273
PG 0844+349	1.18e−15	0.10			1.21e−14	1.00			7.80e−15	0.64	2610
Mrk 110			1.64e−15	0.53	3.11e−15	1.00			3.92e−15	1.26	1370
Mrk 509					3.50e−14	1.00			2.01e−14	0.57	2874
Ark 120			1.62e−14	0.27	5.97e−14	1.00			3.46e−14	0.58	4412
Mrk 817			5.71e−15	0.82	6.94e−15	1.00			2.18e−15	0.31	2186
Mrk 290			3.17e−15	1.63	1.94e−15	1.00					3382
H 2106−099			3.47e−15	0.21	1.65e−14	1.00			9.80e−15	0.59	2241
Mrk 335			6.31e−15	0.33	1.90e−14	1.00			1.24e−14	0.65	1772
Mrk 590					5.89e−15	1.00					2168
Ark 564			4.16e−15	0.29	1.43e−14	1.00	6.45e−15	0.45	6.08e−15	0.43	566
Mrk 79			1.97e−15	0.34	5.84e−15	1.00			1.16e−14	1.99	2271
NGC 7469			5.26e−15	0.59	8.88e−15	1.00					819
H 1934−063			8.54e−15	0.36	2.34e−14	1.00	1.42e−14	0.61	1.63e−14	0.70	1141
NGC 4593			5.82e−15	0.53	1.10e−14	1.00					3406
NGC 3227			1.28e−14	0.70	1.82e−14	1.00					2677
NGC 4151			3.80e−15	0.98	3.87e−15	1.00					835

*observed flux ratio relative to the Fe II 1.0491+1.0502 μm blend (expected theoretical value given below in parenthesis)

**excludes Fe II λ4668

TABLE 7

NEAR-INFRARED NARROW EMISSION LINES

Object Name	[Fe II] λ8617 flux [erg/s/cm^2]	[S III] λ9531 flux [erg/s/cm^2]	[C I] λ9824 flux [erg/s/cm^2]	[C I] λ9850 flux [erg/s/cm^2]	[S VIII] λ9911 flux [erg/s/cm^2]	[S II] 1.0287 μm flux [erg/s/cm^2]	[S II] 1.0320 μm flux [erg/s/cm^2]	[S II] 1.0336 μm flux [erg/s/cm^2]	[S II] 1.0371 μm flux [erg/s/cm^2]
(1)	(2)	(3)	(4)	(5)	(6)	(7)	(8)	(9)	(10)
IRAS 1750+508		7.36e−15							
H 1821+643		1.25e−14							
PDS 456		2.81e−15			4.47e−16			1.74e−15	
3C 273		7.26e−15							
Mrk 876		1.17e−14							
HE 1228+013					9.70e−16				
PG 0844+349		4.57e−15		1.55e−15	1.47e−15		1.21e−15		
Mrk 110		1.70e−14			2.88e−15				
Mrk 509		4.25e−14	4.54e−16	1.12e−15	1.58e−15	5.68e−16	1.81e−15	2.02e−15	3.61e−16
Ark 120		2.61e−14							
Mrk 817		2.28e−14	7.57e−16	1.81e−15	2.10e−15	5.59e−16	3.84e−16	1.02e−16	1.80e−16
Mrk 290		3.33e−14	3.77e−16	9.60e−16	3.16e−15	1.25e−15	1.86e−15	4.12e−16	1.66e−16
H 2106−099		2.25e−14	3.38e−16	1.24e−15	1.39e−15	1.75e−16	1.27e−15	3.24e−16	
Mrk 335		1.31e−14	5.80e−16	4.96e−16	1.22e−15	2.24e−16	5.18e−16	2.66e−16	
Mrk 590		1.10e−14	2.93e−16	1.31e−15		1.68e−16	2.34e−16	1.44e−15	8.24e−17
Ark 564	9.15e−16	3.22e−14	1.99e−16	1.30e−15	4.82e−15	1.21e−15	1.22e−15	1.83e−15	8.77e−16
Mrk 79		5.09e−14	1.09e−15	1.94e−15	4.74e−15	1.25e−15	1.35e−15	5.93e−16	1.47e−16
NGC 5548	3.22e−15	6.59e−14	1.03e−15	8.30e−16	5.60e−15	3.39e−15	7.06e−15	5.65e−16	
NGC 7469		1.16e−13	5.24e−15	1.00e−14	7.67e−15	4.74e−15	5.55e−15	1.03e−15	1.59e−15
H 1934−063	1.59e−15	1.14e−13	3.12e−15	3.68e−15	9.94e−15	2.11e−15	3.80e−15	9.66e−16	7.23e−16
NGC 4593		2.89e−14	5.52e−16	3.73e−16	4.43e−15	3.29e−16	7.62e−16	3.84e−16	
NGC 3227	2.64e−14	3.25e−13	6.53e−15	2.00e−14	3.44e−15	1.45e−14	7.95e−15	1.37e−14	2.88e−15
NGC 4151	3.92e−14	1.16e−12	2.73e−15	1.65e−14	3.82e−14	4.83e−14	5.94e−14	4.17e−14	1.88e−14

TABLE 7—*Continued*

Object Name	[N I] 1.0398 μm flux [erg/s/cm^2]	[N I] 1.0407 μm flux [erg/s/cm^2]	[S IX] 1.2520 μm flux [erg/s/cm^2]	[Fe II] 1.2567 μm flux [erg/s/cm^2]	[Fe II] 1.2788 μm flux [erg/s/cm^2]	[Fe II] 1.3206 μm flux [erg/s/cm^2]	H$_2$ 2.1213 μm flux [erg/s/cm^2]	H$_2$ 2.2230 μm flux [erg/s/cm^2]	H$_2$ 2.2470 μm flux [erg/s/cm^2]
(1)	(11)	(12)	(13)	(14)	(15)	(16)	(17)	(18)	(19)
IRAS 1750+508				7.31e−16					
H 1821+643			1.86e−16	1.68e−15					
PDS 456		2.79e−16		1.92e−15					
3C 273									
Mrk 876			2.09e−16	6.37e−16	8.52e−16		2.09e−15		
HE 1228+013				1.12e−15			5.46e−16		
PG 0844+349			6.39e−16				4.08e−16		
Mrk 110			2.95e−15	4.41e−15			1.12e−15	3.74e−16	
Mrk 509			5.44e−16	2.85e−15			1.79e−15	4.94e−16	3.42e−16
Ark 120				2.32e−15					
Mrk 817	3.42e−16	1.77e−15	6.93e−16	6.40e−16			1.58e−15	3.61e−16	
Mrk 290	1.91e−16		1.30e−15	2.95e−15	7.10e−16		5.07e−16	1.39e−16	
H 2106−099	6.02e−16	1.95e−16	3.96e−15	2.46e−15			7.32e−16		
Mrk 335			1.96e−15	1.79e−15			1.63e−15		
Mrk 590	8.11e−17	4.32e−16	4.60e−16	1.19e−15			3.77e−16		
Ark 564	1.14e−15	1.58e−15	7.17e−15	3.07e−15			1.29e−15		
Mrk 79		4.55e−16	6.44e−15	3.27e−15			4.76e−15	9.26e−16	7.30e−16
NGC 5548	1.09e−15	1.00e−15	2.61e−15	5.96e−16	8.93e−16	8.86e−16	1.41e−15	3.76e−16	
NGC 7469	8.44e−16	8.73e−16	1.96e−15	1.87e−14		6.54e−15	1.02e−14	2.61e−15	1.74e−15
H 1934−063			1.34e−14	9.00e−15		2.47e−15	9.40e−16	1.69e−16	
NGC 4593	2.82e−16	2.85e−16	6.89e−15	1.48e−15			2.66e−15	1.82e−15	
NGC 3227	5.81e−16	6.47e−16		6.69e−14		2.49e−14	3.28e−14	9.19e−15	5.42e−15
NGC 4151	1.22e−14	1.07e−14	3.09e−14	1.22e−13		4.20e−14	1.56e−14	5.90e−15	1.74e−15

TABLE 8

OXYGEN EMISSION LINE RATIOS

Object Name (1)	O I λ8446 broad flux [erg/s/cm^2] (2)	photon flux O I 1.1287/ λ8446 (3)	O I 1.3165 μm broad flux [erg/s/cm^2] (4)	photon flux O I 1.3165/ λ8446 (5)	O I λ7774 broad flux [erg/s/cm^2] (6)	photon flux O I λ7774/ λ8446[*] (7)
IRAS 1750+508	1.47e−14	0.75	4.65e−16	0.05	3.41e−15	1.07
H 1821+643	8.00e−14	0.81	−[**]	−	2.25e−14	1.36
PDS 456	1.86e−13	0.19	−	−	3.94e−14	0.24
3C 273	2.43e−13	0.76	1.84e−14	0.12	6.13e−14	1.93
Mrk 876	4.72e−14	0.48	−	−	3.21e−14	1.21
HE 1228+013	3.79e−14	0.84	2.15e−15	0.09	1.35e−14	4.69
PG 0844+349	3.72e−14	0.81	?[***]	?	8.84e−15	1.15
Ark 564	4.10e−14	0.73	>1.83e-16	>0.01	?	?
H 1934−063	1.02e−13	0.70	7.78e−15	0.12	?	?

[*]after subtracting the contribution from fluorescence

[**]−: not detected

[***]?: not covered by the spectrum

TABLE 9

FE II EMISSION LINE RATIOS

	log (λ4440 − 4700/ 1.0491+1.0502 μm)			log (λ4440 − 4700/ 1.1126 μm)			log (λ8150 − 8365/ 1.0491+1.0502 μm)			log (λ8150 − 8365/ 1.1126 μm)		
	N (1)	mean (2)	$\sigma^\star$ (3)	N (4)	mean (5)	$\sigma^\star$ (6)	N (7)	mean (8)	$\sigma^\star$ (9)	N (10)	mean (11)	$\sigma^\star$ (12)
observed												
all	21	1.40±0.06	6	14	1.54±0.07	<1	21	0.44±0.07	5	14	0.61±0.05	<1
most reliable	11	1.21±0.07	2	11	1.49±0.07	1	11	0.31±0.09	2	11	0.58±0.06	<1
predicted	1.04			1.56			0.11			0.62		
	log (λ4440 − 4700/ λ8150 − 8365)			log (λ9407/ 1.0491+1.0502 μm)			log (λ9573/ 1.0491+1.0502 μm)			log (λ9956 + 9998/ 1.0491+1.0502 μm)		
	N (13)	mean (14)	$\sigma^\star$ (15)	N (16)	mean (17)	$\sigma^\star$ (18)	N (19)	mean (20)	$\sigma^\star$ (21)	N (22)	mean (23)	$\sigma^\star$ (24)
observed												
all	21	0.98±0.06	<1	10	−0.47±0.12	<1	9	−0.91±0.14	3	21	0.17±0.07	3
most reliable	11	0.91±0.08	<1	6	−0.56±0.18	<1	7	−0.96±0.18	2	11	0.09±0.06	3
predicted	0.93			−0.40			−0.54			−0.06		
	log (λ9956 + 9998/ 1.1126 μm)			log (1.0174 μm/ 1.0491+1.0502 μm)			log (1.0174 μm/ 1.1126 μm)			log (1.1126 μm/ 1.0491+1.0502 μm)		
	N (25)	mean (26)	$\sigma^\star$ (27)	N (28)	mean (29)	$\sigma^\star$ (30)	N (31)	mean (32)	$\sigma^\star$ (33)	N (34)	mean (35)	$\sigma^\star$ (36)
observed												
all	14	0.34±0.05	2	13	−0.31±0.07	11	8	−0.28±0.12	2	14	−0.25±0.07	4
most reliable	11	0.36±0.06	2	5	−0.48±0.07	8	5	−0.32±0.05	4	11	−0.28±0.06	4
predicted	0.46			−1.05			−0.53			−0.52		

[*]statistical significance of the difference between mean and predicted values

TABLE 10
UNIDENTIFIED NEAR-INFRARED EMISSION LINES

Object Name (1)	$\lambda 7161$ flux [erg/s/cm^2] (2)	$\lambda 7875 + 7896$ flux [erg/s/cm^2] (3)	$\lambda 10703 + 10736$ flux [erg/s/cm^2] (4)	$\lambda 16890$ flux [erg/s/cm^2] (5)	$\lambda 16925$ flux [erg/s/cm^2] (6)	$\lambda 17004$ flux [erg/s/cm^2] (7)
PDS 456	1.04e−14	5.56e−14	6.52e−14		5.30e−14	2.42e−14
3C 273		3.57e−14				
HE 1228+013		1.46e−14	7.50e−15			
PG 0844+349		2.08e−14	5.73e−15	1.01e−14		
Mrk 817			6.47e−15	1.26e−14		
Ark 564			1.22e−14	4.62e−15	8.42e−16	2.44e−15
Mrk 79			2.90e−14	4.97e−15	4.26e−15	3.54e−15
H 1934−063			2.13e−14	5.75e−15	2.60e−15	4.85e−15
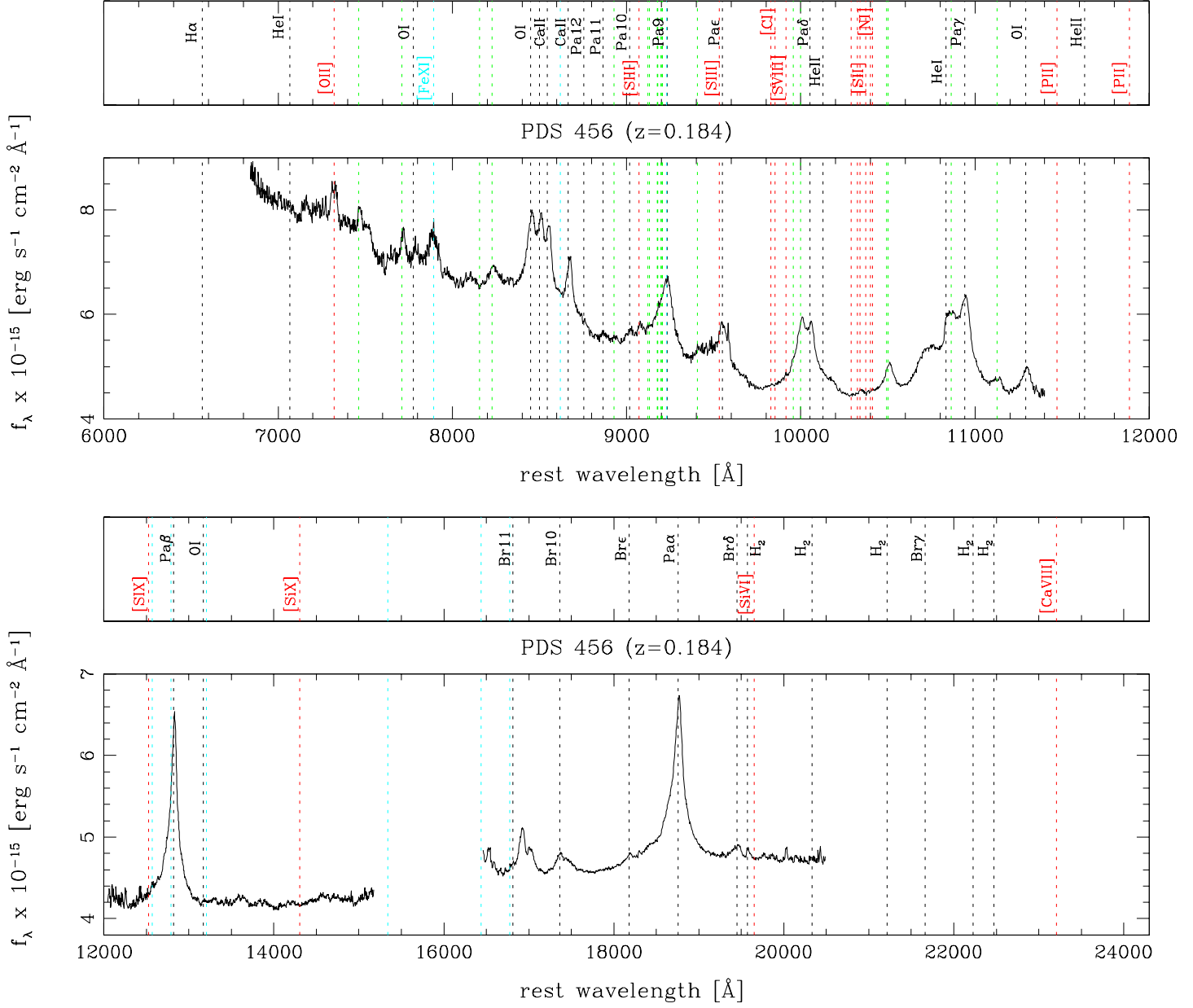
Fig. 1.— IRTF SpeX near-infrared spectrum of PDS 456 shown as observed flux versus rest frame wavelength. Identified emission lines are marked by dotted lines and labeled: black, permitted transitions; green, permitted Fe II multiplets (not labeled); red, forbidden transitions; cyan, forbidden Fe transitions with only those higher than [Fe II] labeled. [*The spectral plots for all sources are available in colour in the electronic edition of the journal. The spectra used to create these plots are available for download as a tar-file.*]
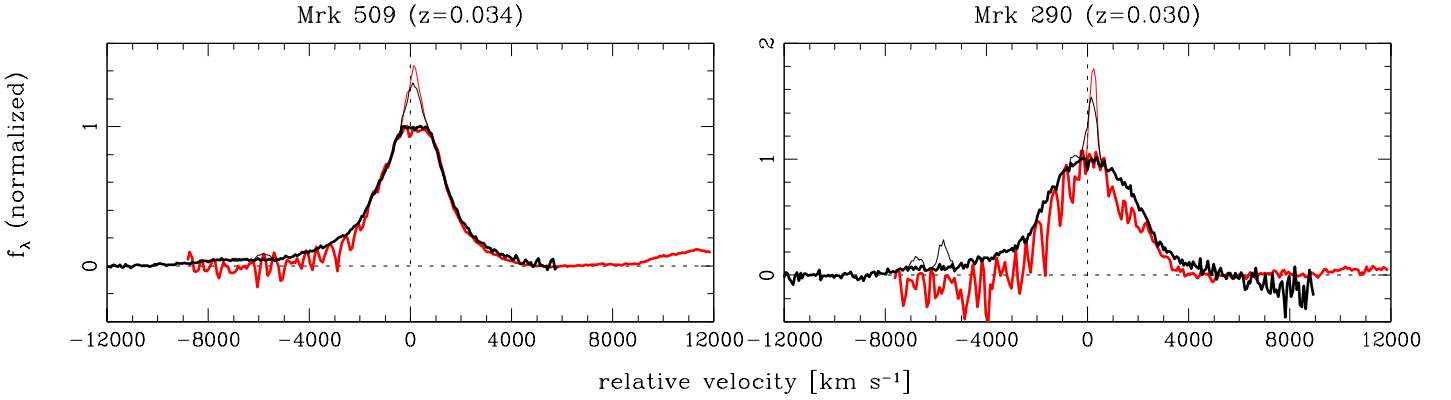
Fig. 2.— IRTF SpeX profiles of the broad emission lines Paα (red) and Paβ (black) in velocity space relative to the expected rest frame wavelength (thick lines). The profiles have been continuum-subtracted and normalized to the same peak intensity (of the broad component). The subtracted blends and narrow components are also shown (thin lines). [*The spectral plots for all sources are available in colour in the electronic edition of the journal.*]
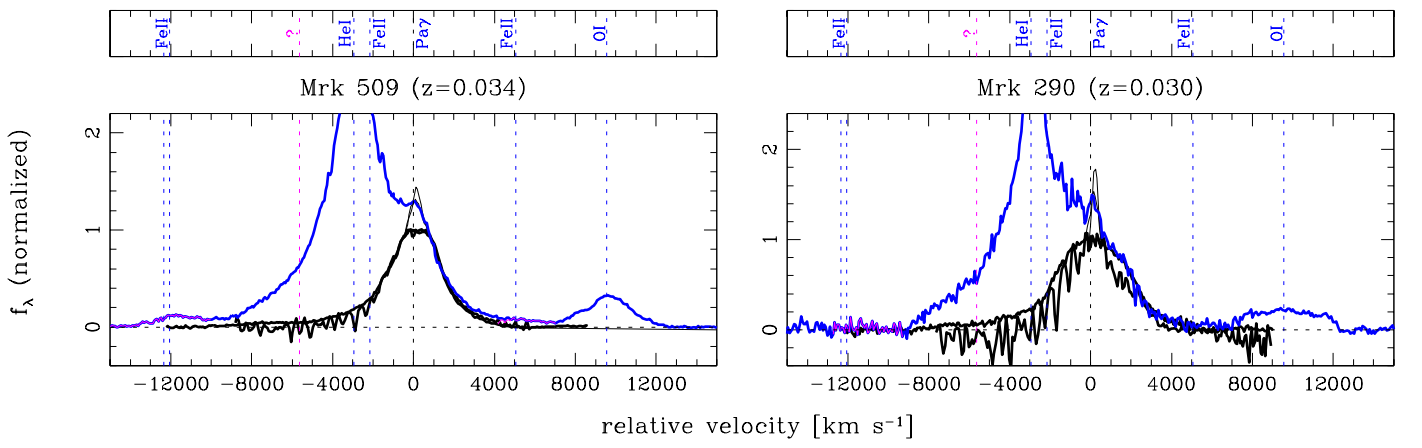

Fig. 3.— IRTF SpeX profiles of the emission line blend Paγ, He I 1.0830 μm, O I 1.1287 μm, Fe II 1.0502 μm, Fe II 1.0863 μm, and Fe II 1.1126 μm (blue, thick lines) compared to the profiles of Paα and Paβ (black). Profiles are shown in velocity space relative to the expected rest frame wavelength indicated by the vertical dotted lines (black for the Paschen lines, blue for He I, O I and Fe II, magenta for the unidentified feature). The profiles have been continuum-subtracted and normalized to the same peak intensity (of the broad component). The isolated Fe II profiles (magenta) are also shown. [*The spectral plots for all sources are available in colour in the electronic edition of the journal.*]
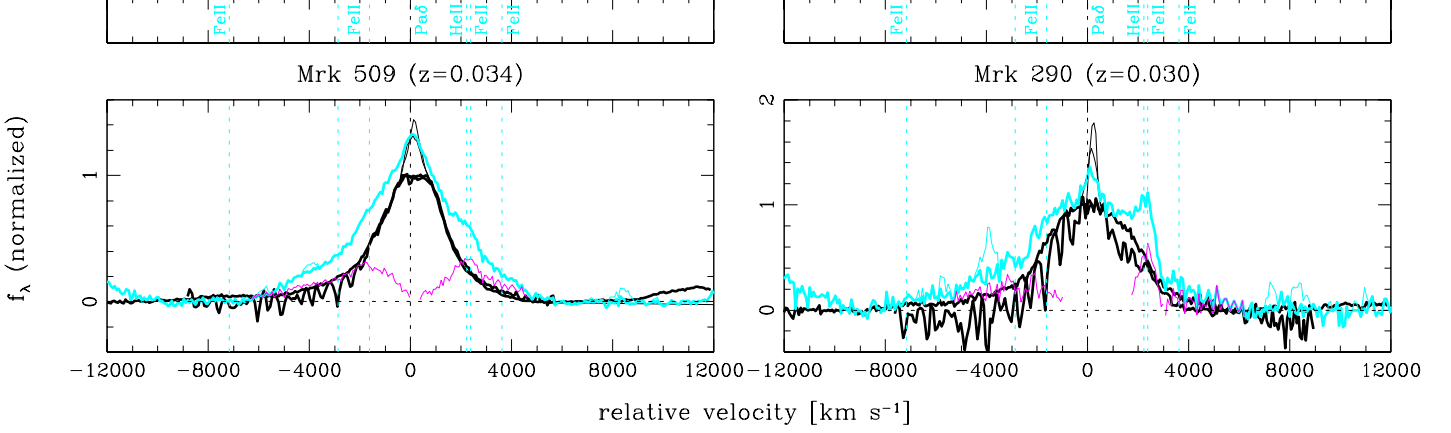
Fig. 4.— IRTF SpeX profiles of the emission line blend Paδ, He II 1.0124 μm, Fe II λ9812, Fe II λ9956 + 9998, Fe II 1.0132 μm, and Fe II 1.0174 μm (cyan, thick lines) compared to the profiles of Paα and Paβ (black). Profiles are shown in velocity space relative to the expected rest frame wavelength indicated by the vertical dotted lines (black for the Paschen lines, cyan for Fe II and He II). The profiles have been continuum-subtracted and normalized to the same peak intensity (of the broad component). The subtracted narrow emission line blends (cyan, thin lines) and the isolated Fe II and He II profiles (magenta) are also shown. [*The spectral plots for all sources are available in colour in the electronic edition of the journal.*]
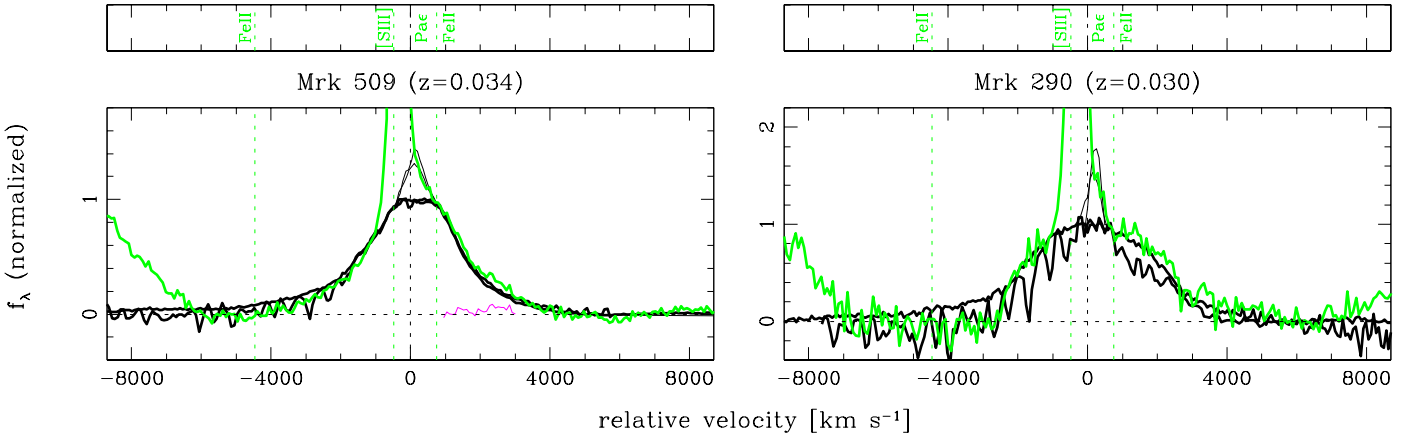
Fig. 5.— IRTF SpeX profiles of the emission line blend Paε, [S III] λ9531, Fe II λ9407, and Fe II λ9573 (green, thick lines) compared to the profiles of Paα and Paβ (black). Profiles are shown in velocity space relative to the expected rest frame wavelength indicated by the vertical dotted lines (black for the Paschen lines, green for Fe II and [S III]). The profiles have been continuum-subtracted and normalized to the same peak intensity (of the broad component). The isolated Fe II profiles (magenta) are also shown. [*The spectral plots for all sources are available in colour in the electronic edition of the journal.*]
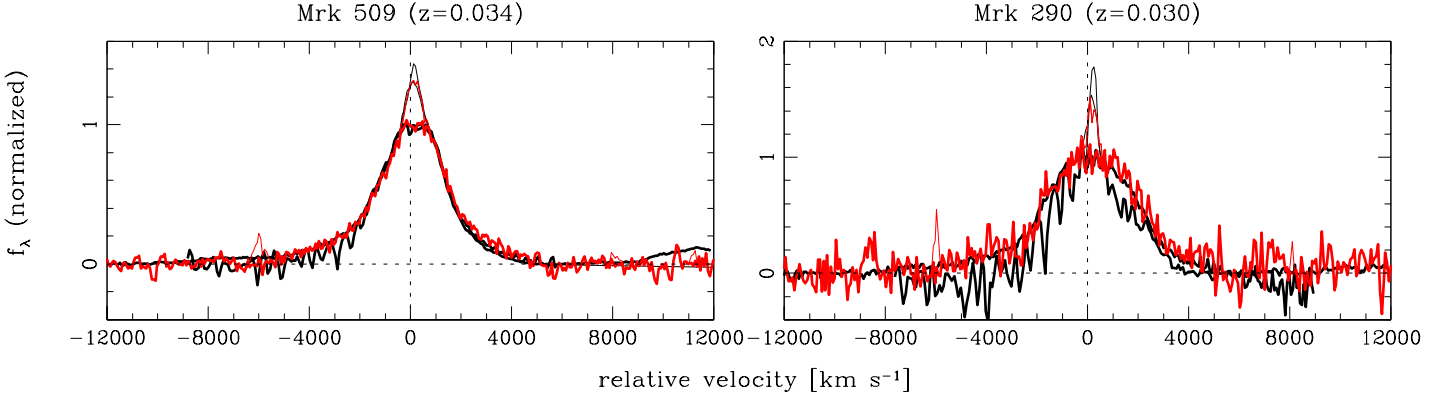
Fig. 6.— IRTF SpeX profiles of the broad emission line Brγ (red) compared to the profiles of Paα and Paβ (black) in velocity space relative to the expected rest frame wavelength (thick lines). The profiles have been continuum-subtracted and normalized to the same peak intensity (of the broad component). The subtracted blends and narrow components are also shown (thin lines). [*The spectral plots for all sources are available in colour in the electronic edition of the journal.*]
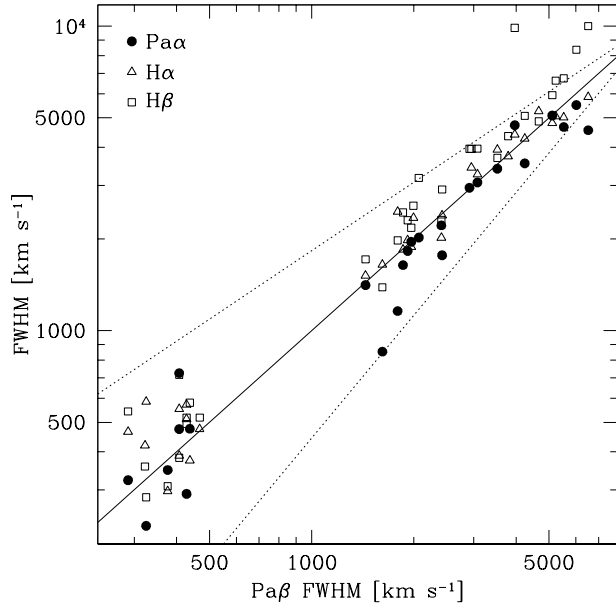
Fig. 7.— The full width at half maximum (FWHM) of the broad and narrow *inflected* components (upper right and lower left symbols, respectively) of Paβ vs. Paα (filled circles), Hα (open triangles), and Hβ (open squares). The compared emission lines have similar widths (solid line) within the error range given by the spectral resolution (dotted lines). However, in several sources the broad Paα component suffers slightly from atmospheric absorption, and there is a trend for the Hβ broad component to be wider than that of Paβ. The latter effect is most likely due to the presence of the Hβ "red shelf".
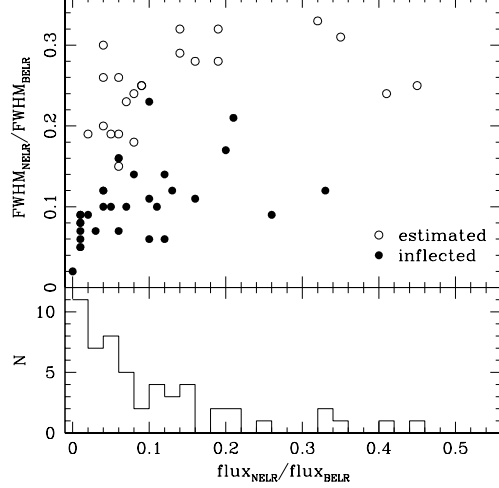
Fig. 8.— Upper panel: The ratio between the full width at half maximum (FWHM) of the narrow and broad components versus their flux ratios for the cases where the narrow component was inflected (filled circles) and estimated (open circles). Included are the emission lines Paβ, Hα and Hβ. Lower panel: A histogram of the flux ratios between the narrow and broad components plotted in the upper panel.
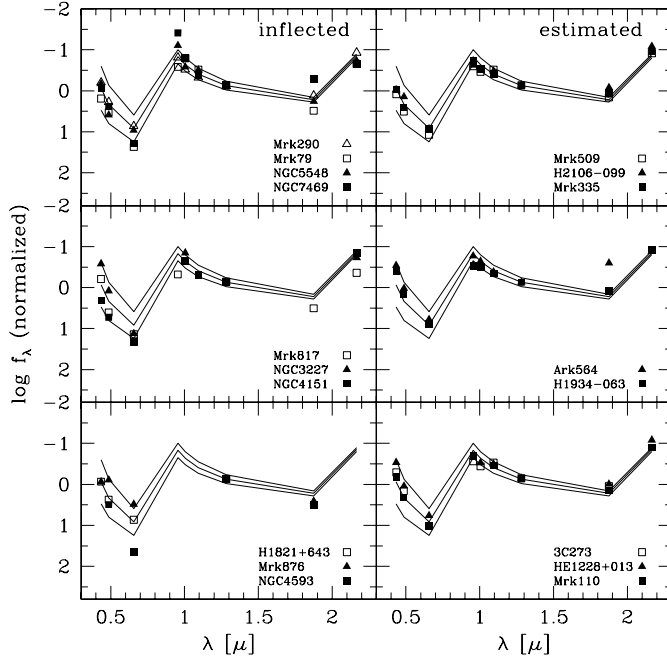
Fig. 9.— Narrow component emission line fluxes compared to expectations from Case B recombination (for a temperature of $T = 15000$ K and an electron density of $n_e = 10^4$ cm^{-3}). From bottom to top the dust extinction assumed was $A_V = 0, 1$ and 2 mag. The measurement points and the Case B solid lines were normalized to the flux of Paβ.
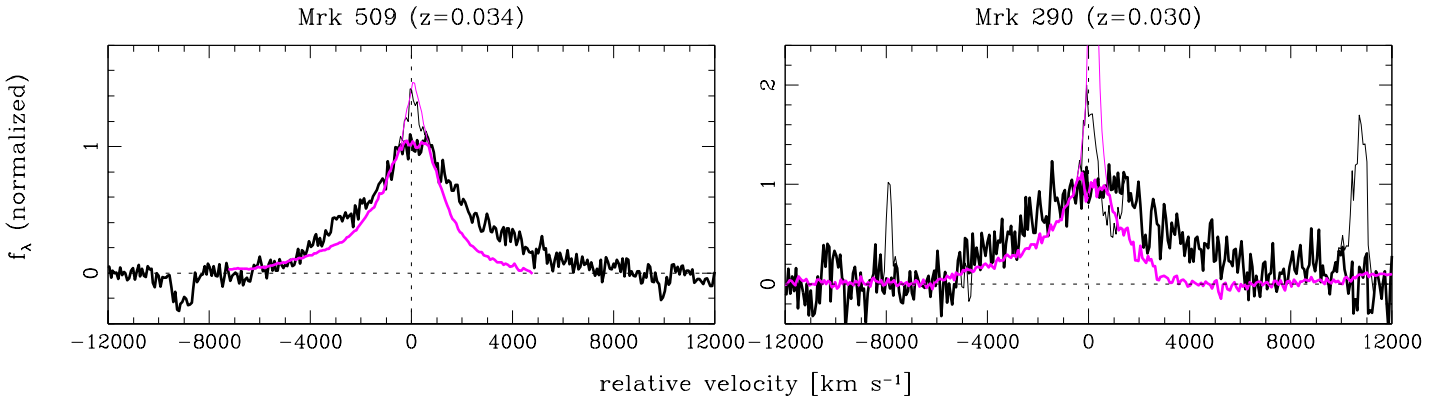
Fig. 10.— Profiles of the broad emission lines He I λ5876 (black) and He I 1.0830 μm (magenta) in velocity space relative to the expected rest frame wavelength (thick lines). The profiles have been continuum-subtracted and normalized to the same peak intensity (of the broad component). The subtracted blends and narrow components are also shown (thin lines).
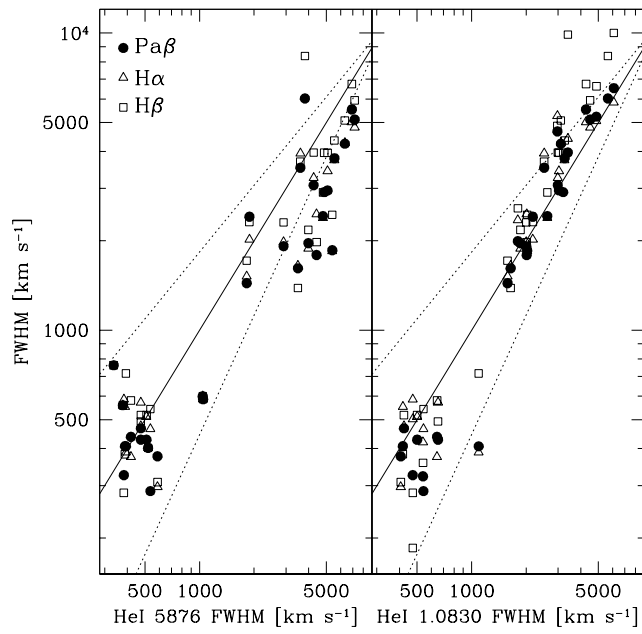
Fig. 11.— The full width at half maximum (FWHM) of the broad and narrow *inflected* components (upper right and lower left symbols, respectively) of He I λ5876 and He I 1.0830 μm vs. the hydrogen emission lines Paβ, Hα, and Hβ (filled circles, open triangles, and open squares, respectively). Emission lines are considered to have similar widths (solid line) if they lie within the error range given by the spectral resolution (dotted lines).
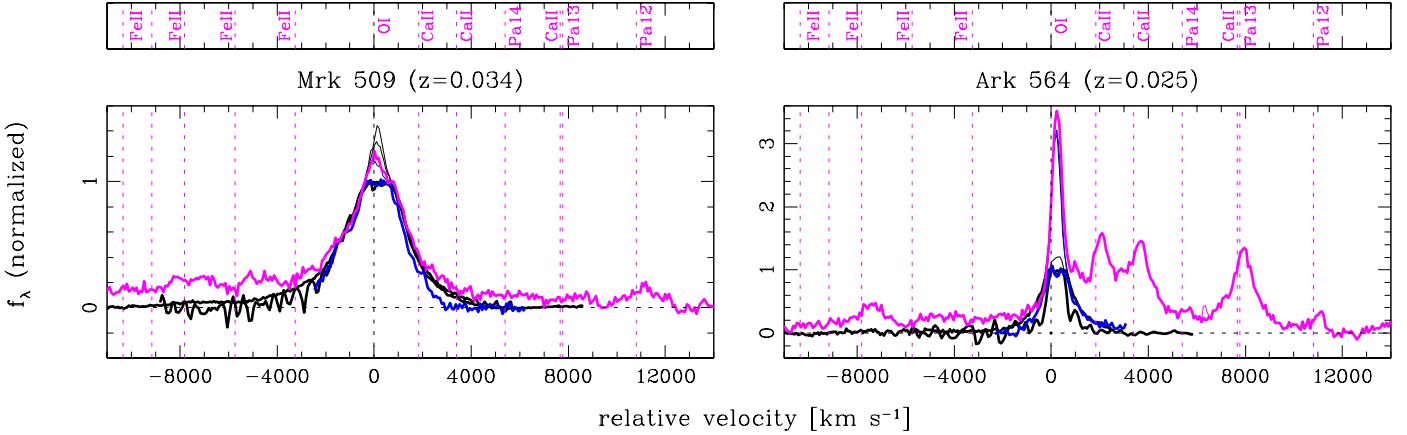
Fig. 12.— IRTF SpeX profiles of the broad emission lines O I λ8446 (magenta) and O I 1.1287 μm (blue) compared to the profiles of Paα and Paβ (black) in velocity space relative to the expected rest frame wavelength (thick lines). The O I λ8446 emission line blends with the IR Fe II 'hump', Ca II triplet, Pa14, Pa13, and Pa12 (magenta vertical dotted lines). The profiles have been continuum-subtracted and normalized to the same peak intensity (of the broad component). The subtracted narrow components and blends of narrow emission lines are also shown (thin lines). [*The spectral plots for all sources are available in colour in the electronic edition of the journal.*]
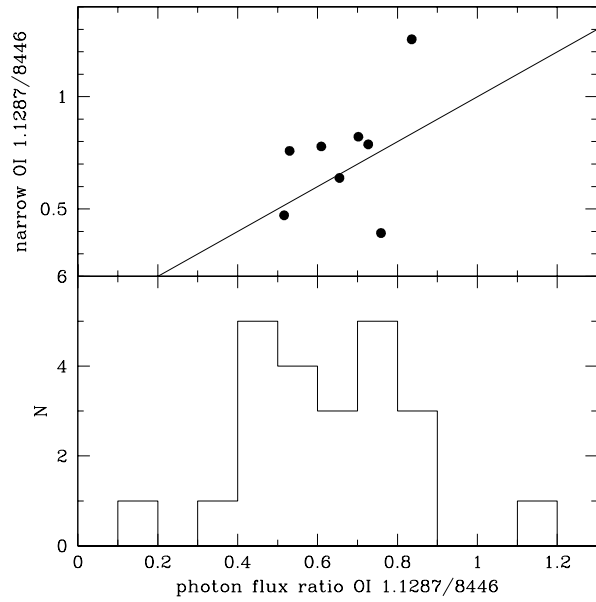
Fig. 13.— Lower panel: The distribution of the photon flux ratios between the O I 1.1287 μ and O I λ8446 emission lines for the broad components. Upper panel: The photon flux ratios between the broad components of the O I 1.1287 μ and O I λ8446 emission lines vs. those of the narrow components.
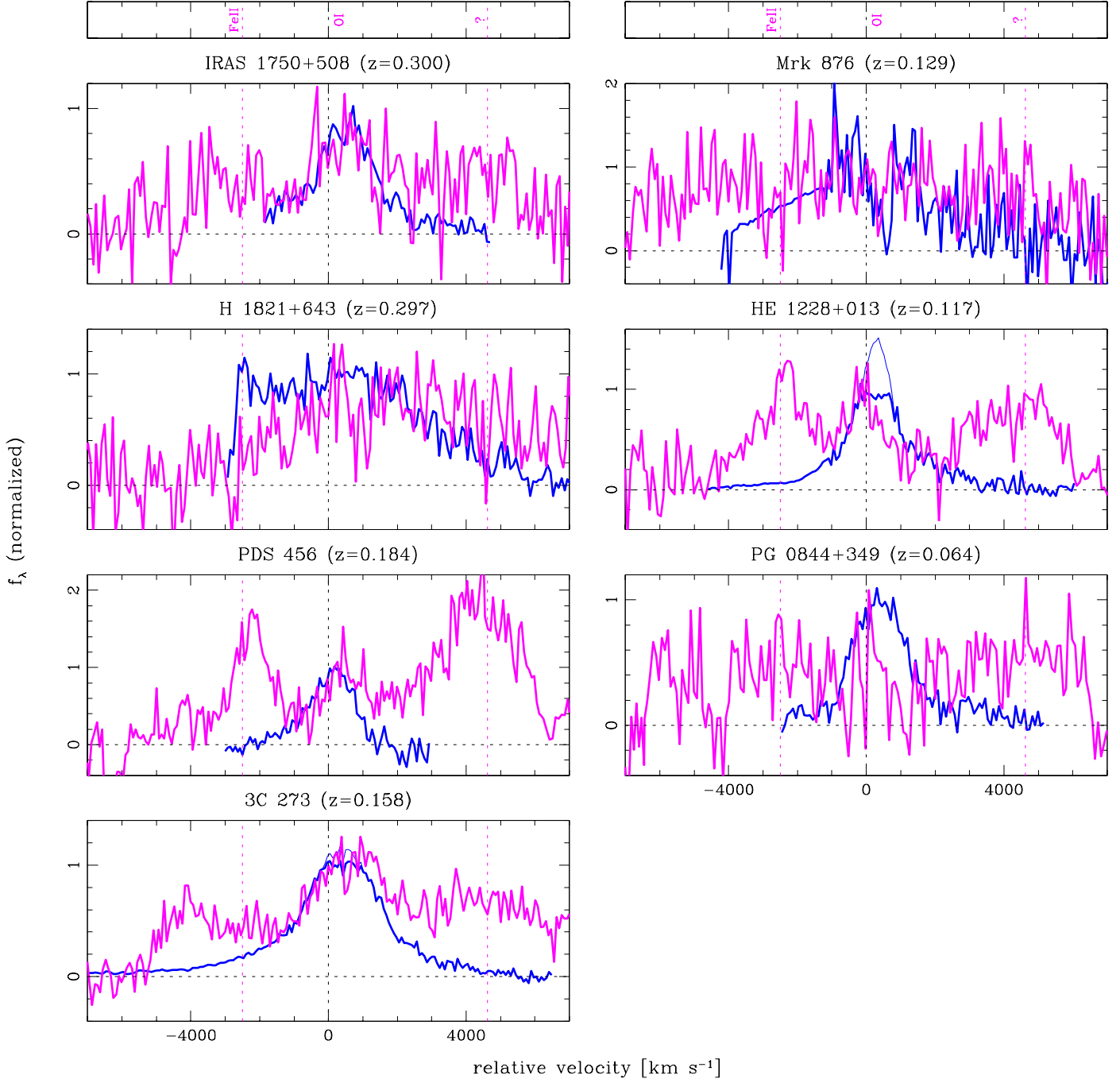
Fig. 14.— IRTF SpeX profiles of the broad emission lines O I λ7774 (magenta) and O I 1.1287 μm (blue) in velocity space relative to the expected rest frame wavelength (thick lines). The O I λ7774 emission line blends with Fe II λ7712 and an unidentified feature (magenta vertical dotted lines). The profiles have been continuum-subtracted and normalized to the same peak intensity (of the broad component). The narrow components of O I 1.1287 μm are also shown (blue thin lines).
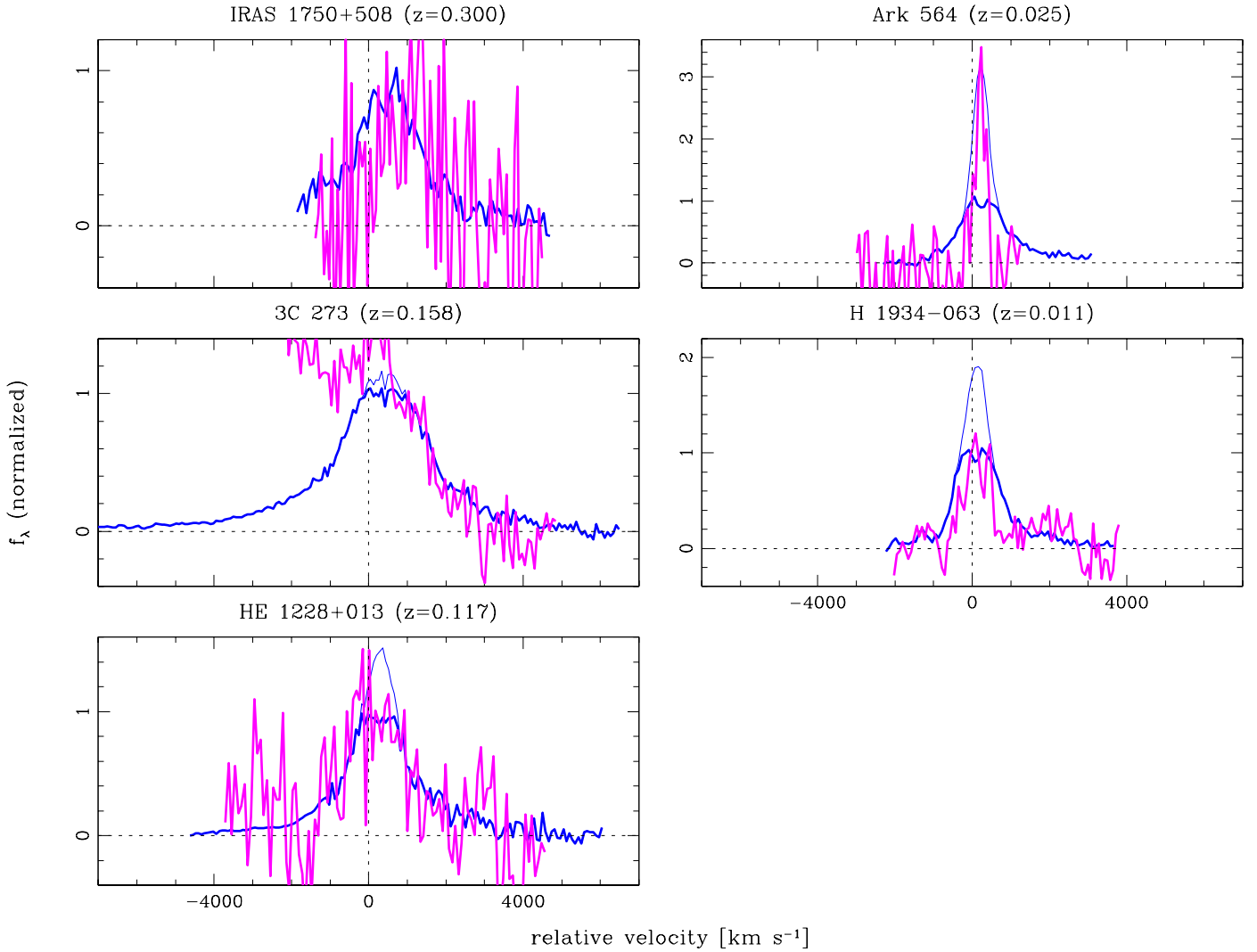
Fig. 15.— IRTF SpeX profiles of the broad emission lines O I 1.3165 μm (magenta) and O I 1.1287 μm (blue) in velocity space relative to the expected rest frame wavelength (thick lines). The profiles have been continuum-subtracted and normalized to the same peak intensity (of the broad component). The subtracted narrow components of O I 1.1287 μm are also shown (blue thin lines).
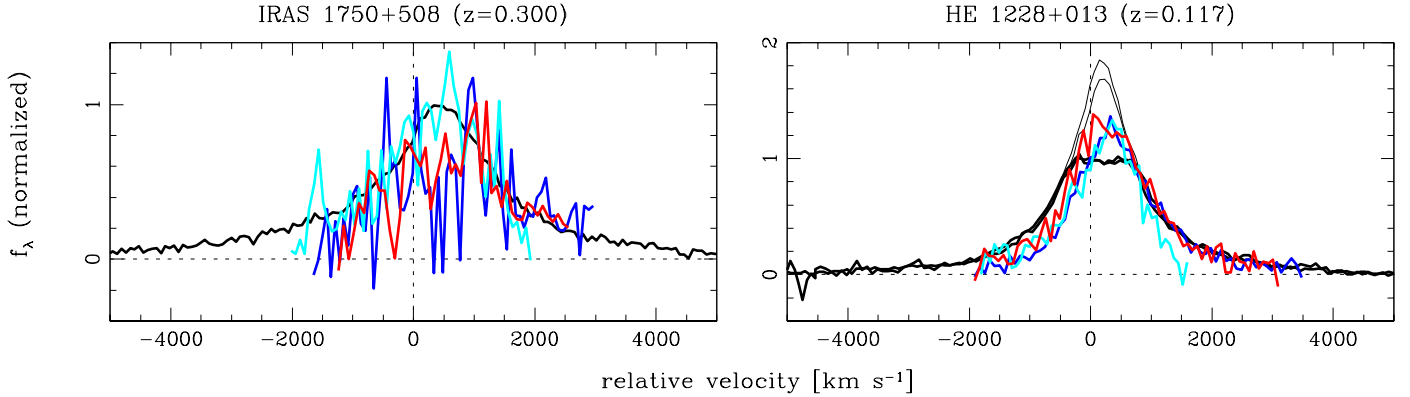
Fig. 16.— IRTF SpeX profiles of the iron emission lines Fe II 9956 + 9998 (cyan), Fe II 1.0491+1.0502 μm (blue), and Fe II 1.1126 μm (red) compared to the profiles of Paα and Paβ (black) in velocity space relative to the expected rest frame wavelength (thick lines). The profiles have been continuum-subtracted and normalized to the same peak intensity (of the broad component). The subtracted narrow components of the Paschen lines are also shown (thin lines). [*The spectral plots for all sources are available in colour in the electronic edition of the journal.*]
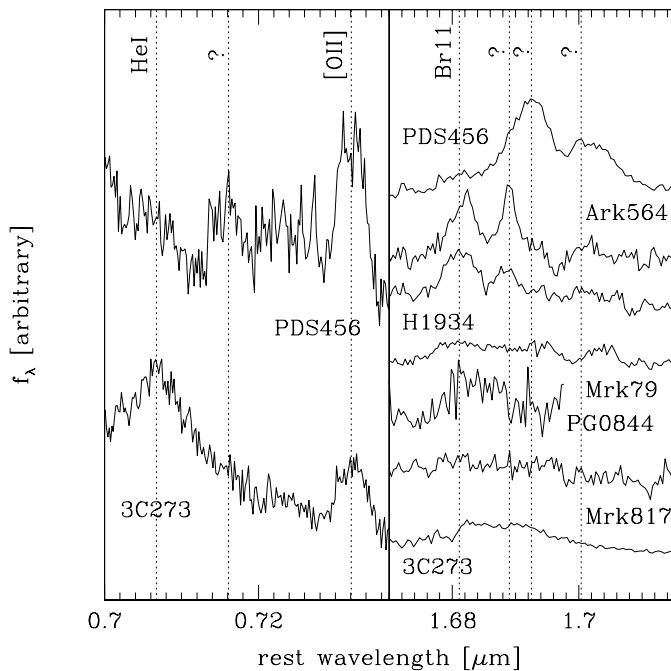

Fig. 17.— IRTF SpeX profiles of the unidentified emission features at 7161 Å (left panel) and at 16890 Å, 16925 Å, and 17004 Å (right panel).